

# Experimental investigation of the water entry and/or exit of axisymmetric bodies

Thibaut Breton<sup>1,2</sup>, A. Tassin<sup>1,†</sup> and N. Jacques<sup>2</sup>

<sup>1</sup>Ifremer, RDT, F-29280 Plouzané, France

<sup>2</sup>ENSTA Bretagne, UMR CNRS 6027, IRDL, 29806 Brest CEDEX 09, France

(Received 8 July 2019; revised 20 March 2020; accepted 6 July 2020)

This paper presents an experimental investigation of the evolution of the wetted surface and of the hydrodynamic force during the water exit of a body initially floating at the water surface, and during combined water entry and exit. The evolution of the surface of contact between the body and the water is measured using transparent mock-ups and an LED edge-lighting system. This technique makes it possible to follow the evolution of the wetted surface during both the entry and exit phases with a high-speed video camera placed above the mock-up. The feasibility of the technique is shown for different axisymmetric bodies: a circular disc, a cone and a sphere. The evolution of the hydrodynamic force and of the radius of the wetted surface measured during the experiments are compared with theoretical results obtained with a combined Wagner-modified von Karman approach (Tassin *et al. J. Fluids Struct.*, vol. 40, 2013, pp. 317–336), the linearized water exit model of Korobkin *et al. (J. Fluids Struct.*, vol. 69, 2017*a*, pp. 16–33) and the small-time self-similar solution of Korobkin *et al. (J. Engng Maths*, vol. 102, 2017*b*, pp. 117–130).

**Key words:** free-surface flows, wave–structure interactions

---

## 1. Introduction

The water exit phenomenon designates the upward lifting of a body initially floating at the water surface or the lifting of a body which previously entered the water. One may speak of a combined water entry and exit event in the latter case. Studies of this hydrodynamic phenomenon are motivated by various marine applications such as wave impact on offshore platforms (Baarholm & Faltinsen 2004) and on suspended structures (Sun & Helmers 2015), or ship slamming (Kaplan 1987). The aeronautical industry has also to deal with water entry and exit to predict the hydrodynamic loads acting on the fuselage of an airplane during emergency landing (see Bensch *et al.* 2001; Tassin *et al.* 2013). It is also interesting to note that one of the first experimental studies of the water exit phenomenon was conducted by researchers in biomechanics in order to understand the cat lapping phenomenon (Reis *et al.* 2010).

Both water entry and water exit involve a rapid evolution of the surface of contact between the body and the liquid, which is also called the wetted surface. Following the definition commonly adopted in water entry problems (see Korobkin 2007), the contact

† Email address for correspondence: [alan.tassin@ifremer.fr](mailto:alan.tassin@ifremer.fr)

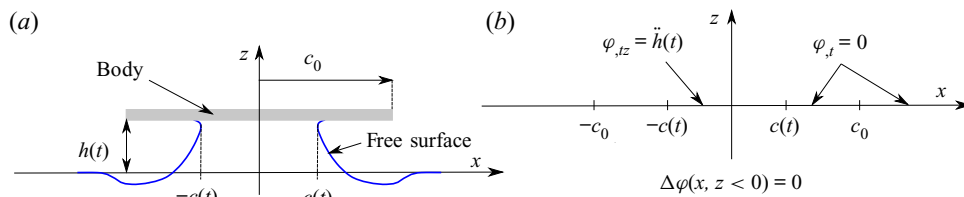


FIGURE 1. Water exit of a flat plate and linearized water exit problem. (a) Water exit of a flat plate. (b) Linearized mixed boundary value problem satisfied by the velocity potential  $\varphi$  in Tassin *et al.* (2013) and Korobkin (2013).

surface designates the surface delimited by the line(s) where the free surface is vertical,  $|x| = c(t)$  in the two-dimensional case illustrated in figure 1(a). During an entry stage the contact surface is in expansion whereas the contact surface is contracting during an exit stage. In general, during the water entry and exit of a rigid body moving vertically, the water entry (respectively water exit) stage corresponds to the period during which the body moves downward (respectively upward). In the case of entry with deceleration and then exit, suction loads (hydrodynamic pressures being below the atmospheric pressure) arise during the entry stage and the hydrodynamic force remains negative (directed downward) during most of the exit stage. Also, when the body deceleration is constant, the maximum suction force occurs at the transition between the entry stage and the exit stage (Tassin *et al.* 2013). However, when dealing with the complex motion of highly deformable bodies, the notion of entry or exit is less obvious and we suggest defining the entry and exit stages based on the evolution of the contact point (which is not known *a priori*). Note that in the numerical simulations of Piro & Maki (2013*b*) corresponding to the water entry and exit of a rigid wedge with separation occurring at the knuckle, the water starts separating from the surface of the body while the wedge is still going downward (see figure 7, right column, second row, in Piro & Maki 2013*b*). As a consequence, the maximum suction force occurs before the wedge starts going up again (see figure 9(b) in Piro & Maki 2013*b*). The suction load and the separation of the liquid from the body surface are two important features characterizing the water exit phenomenon, but they can be observed in other multiphase problems. Indeed, suction and flow separation are observed during the oblique water entry of wedges and curved bodies at high horizontal speed (see Semenov & Yoon 2009; Reinhard, Korobkin & Cooker 2012; Reinhard 2013). The magnitude of the suction loads can lead to cavitation on the fuselage of an aircraft (Iafrazi & Grizzi 2019). Flow separation also occurs during the vertical water entry of curved bodies (e.g. sphere, cylinder) when the entry speed is sufficiently large (Duez *et al.* 2008). These examples show that flow separation and suction are closely related. The water exit problem is a good case study in order to investigate the suction and flow separation phenomena. A better understanding of the water exit phenomenon would probably help understanding the other mentioned phenomena involving suction and flow separation.

Very few studies have been dedicated to the water exit problem in comparison with the extensive research on the water entry problem. Most of the investigations were so far based on analytical and numerical approaches. To the authors' knowledge, the first analytical model aiming at modelling the exit stage (subsequent to an entry stage) was proposed by Kaplan (1987). In this model, the entry stage was modelled with the original Wagner model (Wagner 1931, 1932) and the Wagner model was modified in order to make it compatible with the exit stage. This modification consisted in disregarding the 'slamming term' and retaining only the 'added mass' term in the Wagner model when calculating the hydrodynamic force during the exit stage. A similar approach was later

used by Bensch *et al.* (2001) and Baarholm & Faltinsen (2004). More recently, Tassin *et al.* (2013) and Korobkin (2013) showed that a similar result could be obtained by solving the linearized mixed boundary value problem described in figure 1(b) (where  $\varphi$  is the velocity potential) and by enforcing the Kutta-type condition  $\varphi_{,t}(|x| = c(t)^-) = 0$  at the contact point during the exit stage (with  $\varphi_{,t}$  the time derivative of  $\varphi$ ). A consistent analytical model of water exit shall predict accurately the evolution of the wetted surface and the hydrodynamic force (or pressure distribution). In Tassin *et al.* (2013), the contact point position is determined by a modified von Karman approach in which the boundary of the contact surface corresponds to the geometrical intersection between a horizontal plane of reference and the body surface. The altitude of the reference plane is set to the maximum altitude reached by the contact point during the entry stage (at the transition between entry and exit). The pressure is computed with the modified Logvinovich model, but the only terms which remain during the exit stage depend on the body acceleration (added mass effect). Despite the simplicity of the approach used for the prediction of the contact point position, the results obtained in terms of pressure distribution and hydrodynamic force are in rather good agreement with the reference numerical results during the beginning of the water exit stage (when the suction force is maximal). In the linearized model of Korobkin (2013), a more elaborated condition is used to predict the contact point position. This author assumes that the speed of contraction of the contact surface is proportional to the velocity of the particles located at the contact points. For a symmetric two-dimensional problem in the lower  $x$ - $z$  half-plane ( $z < 0$ ), the contact point condition reads:  $\dot{c}(t) = \gamma \cdot \varphi_{,x}(x = c(t), z = 0)$ , with  $\dot{c}(t)$  the time derivative of the half-width of the wetted surface and  $\varphi_{,x}$  the horizontal gradient of the velocity potential (i.e. the horizontal velocity). Korobkin (2013) found that a value of  $\gamma = 2$  gave a very good prediction of the hydrodynamic force during almost the entire duration of the exit stage. However, the accuracy of the prediction of the contact surface with this value of  $\gamma$  has not been assessed. Note that Korobkin's condition for the evolution of the contact point position was used earlier by Baarholm & Faltinsen (2004) (with  $\gamma = 1$ ) to ensure the stability of their nonlinear potential flow simulations during the exit stage of a wave impact. It is indeed also difficult to accurately simulate numerically water exit problems, especially when the exit is subsequent to a water entry stage. Indeed, the numerical algorithms used in computational fluid dynamics (CFD) are not all able to handle both the entry and the exit stage. For instance, Piro & Maki (2013a) observed that the interface compression scheme, that allows us to improve the accuracy of water entry simulations (with a multiphase CFD approach) leads to free-surface instabilities during water exit. To circumvent this problem, they proposed an adaptative interface compression algorithm in order to improve the simulation of the exit stage. In the finite element methods based on a single phase arbitrary Euler-Lagrange approach, it is common to use a penalty contact algorithm for the simulation of water impact problems (Tassin *et al.* 2012). However, this approach cannot properly handle the suction (i.e. the occurrence of negative relative pressure). The same problem may occur in simulations based on the smoothed particle hydrodynamics method (Panciroli *et al.* 2012).

New experimental studies are necessary to improve our knowledge of the water exit phenomenon, to validate the numerical simulations and to help developing new analytical models. Indeed, to date, very few experimental results are available. Reis *et al.* (2010) conducted their experiments at very low scale on circular discs and without measuring the hydrodynamic force or the evolution of the wetted surface. More recently, Vega-Martínez *et al.* (2019) published experimental results on the water exit of a circular disc, but the elasticity of the disc had a large effect on the results and the measurement of the wetted surface was restricted to the very beginning of the water exit ( $c(t)/c(0) > 0.9$ ).

Based on the above observations on the water exit stage, experimental results in terms of contact surface and hydrodynamic force are of prime interest. For this purpose, we conducted both water exit and combined water entry and exit experiments with axisymmetric bodies (a circular disc, a cone and a spherical cap). The choice of axisymmetric body shapes over two-dimensional bodies was made in order to avoid undesired three-dimensional effects that may appear with a ‘pseudo’-two-dimensional experimental set-up. Indeed, with two-dimensional mock-ups, three-dimensional effects always take place at the extremities of the specimen (e.g. Shams, Zhao & Porfiri 2017). The axisymmetric problem also has the advantage to remain tractable with analytical approaches. Indeed, the analytical models of Tassin *et al.* (2013) and Korobkin (2013) are readily applicable to axisymmetric water exit problems. The different body shapes considered in the present study make it possible to assess the effect of the shape on the water exit phenomenon.

One original aspect of our work is the use of transparent mock-ups and a LED edge-lighting device to track the contour of the contact surface (the contact line) during the experiments. We previously showed the feasibility of this technique for flat plates of different shapes (a circular disc and a square plate) in Tassin *et al.* (2017). This technique was proposed as an alternative to the bottom view approach used in previous water entry experiments (e.g. Halbout 2011), which we found to be inappropriate for the tracking of the contact line during the water exit of a circular disc. We now report on a detailed study on the water exit and combined water entry and exit of different three-dimensional mock-ups, hence demonstrating the applicability of the edge-lighting technique for three-dimensional bodies. More importantly, we show that it is possible to track both the contact line and the jet front during the entry stage. The experiments have been carried out in a medium-scale wave tank with a dedicated metallic frame fixed on a 6 degree-of-freedom motion generator that allows an accurate control of the motion of the mock-ups. Moreover, with this new experimental set-up, it is possible to record simultaneously the evolution of the contact line and the hydrodynamic force. To validate the accuracy of the LED edge-lighting technique, each experiment has been realized with and without a draughtboard placed at the bottom of the wave tank. With this technique inspired from Socolan, Remy & Thibault (2006), the wetted surface corresponds to the region over which the draughtboard appears as undistorted (except for the distortion due to the shape of the body and to the perspective).

Through this experimental study, several aspects of the water exit phenomenon are studied:

- (i) We investigate the influence of the body shape on the water exit problem. In particular, we compare the evolution of the wetted surface and of the hydrodynamic force for the three different shapes (circular disc, cone, sphere), but with the same initial wetted surface and the same experimental conditions.
- (ii) The effect of viscosity and surface tension is assessed by carrying out experiments in Froude similarity with the conical mock-up for different values of the initial wetted surface (by varying the initial penetration depth).
- (iii) The evolution of the wetted surface measured during a water exit experiment is compared with the evolution of the wetted surface measured during the exit stage of a combined water entry and exit experiment.
- (iv) The experimental results are compared with different theoretical models: the combined Wagner-modified von Karman model of Tassin *et al.* (2013), the linearized water exit model of Korobkin, Khabakhpasheva & Maki (2017a) and the small-time self-similar solution of Korobkin, Khabakhpasheva &

Rodríguez-Rodríguez (2017*b*). For this purpose, an extension of the linearized model of Korobkin *et al.* (2017*a*) to the water exit of a rigid axisymmetric body with an arbitrary exit kinematics ( $\dot{h}(t) \geq 0$ ) was implemented.

The article is organized as follows: § 2 describes the experimental set-up, § 3 explains the method used for the analysis of the measurements, § 4 presents the experimental results, § 5 discusses the effect of different parameters affecting water exit and presents comparisons with theoretical results and finally the conclusions of our study are drawn in § 6. A detailed validation of the LED edge-lighting technique through comparisons with the draughtboard technique is also presented in [appendix A](#).

## 2. Experimental set-up

The experiments were conducted in the wave and current flume of IFREMER in Boulogne-sur-mer (France). Our investigation of the water exit phenomenon motivated the development of a dedicated experimental set-up which is described in [figure 2](#). This set-up is composed of a metallic frame, a transparent mock-up and a 6-degree-of-freedom motion generator (see [figure 2a](#)). The motion generator (hexapod) is used to adjust the inclination of the set-up and to move the set-up vertically during the experiments. The entire set-up is placed above a medium-scale wave tank (2 m deep, 4 m wide and 20 m long) and half-way from the sidewalls of the tank. The evolution of the contact line is recorded by an onboard high-speed video camera (Photron Fastcam Mini AX50) looking downward and fixed to the metallic frame above the centre of the mock-up. As the camera follows the motion of the mock-up, the distance between the camera and the mock-up is constant during the experiments. The images presented in this paper were recorded at a frame rate of 1000 f.p.s. and using a Nikon 20 mm F2.8 lens. The hydrodynamic force was recorded using 3 piezoelectric load cells (Kistler 9331B) connected to a dynamic (and quasi-static) charge amplifier (Kistler LabAmp type 5167A40FK). The load cells were placed between the mock-up and the metallic frame in order to minimize the mass of the elements below the force sensors and which may induce an inertial force component during the experiments. Although we tried to place the force sensors as close as possible to the mock-up and to minimize the mass of the mock-up, inertia forces are unavoidable during water exit experiments because the velocity of the mock-up is not constant. In order to extract the hydrodynamic force component from the total force measured by the sensors, all the experiments were carried out both in air and water with identical motions. This way, it was possible to subtract the inertia force component measured in air (without touching the water) from the force measured during the water entry and/or exit experiments. Note that in pure water entry experiments, inertia effects can be mitigated by enforcing a constant water entry velocity, but it is also common to compensate the variation of velocity during water entry experiments (see el Malki Alaoui *et al.* 2012).

### 2.1. Description of the transparent mock-ups

The technique employed for the visualization of the wetted surface during the experiments is based on the use of transparent mock-ups and a LED edge-lighting technique. Three transparent shells of different shapes were built: a circular disc, a cone and a hemisphere. Note that each mock-up corresponds to an axisymmetric transparent shell which was manufactured in a block of PMMA and finely polished. An array of high-power LEDs was mounted at the periphery of each mock-up in order to diffuse light in the material. The LED array was covered of aluminium cellotape in order to maintain it in position

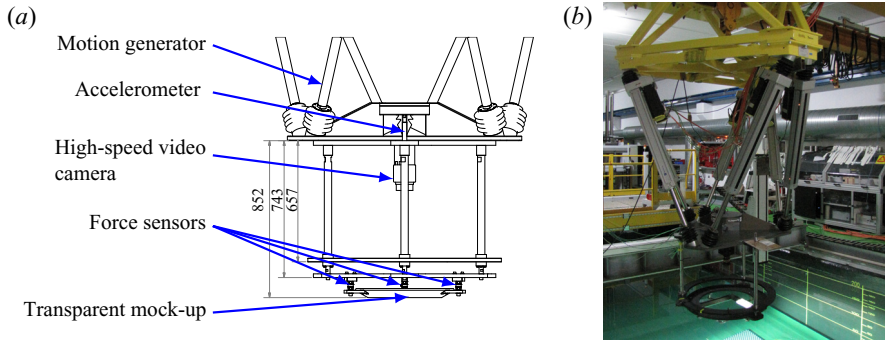


FIGURE 2. Experimental set-up. (a) Sketch of the experimental set-up (dimensions are given in mm). (b) Photograph of the experimental set-up.

and to direct the light toward the mock-up. A vertical cross-section and a picture of each mock-up is displayed in figure 3. In figure 3(a), one can see that the circular disc is composed of a 40 cm central region which is 15 mm thick and a sloped region at the periphery of the mock-up which is 11 mm thick. The disc was continued obliquely with a slope of  $30^\circ$  in order to prevent the LEDs from being in contact with the water. The conical mock-up described in figure 3(c) is composed of a central part with a deadrise angle of  $15^\circ$  and a thickness of 15 mm. For the same reason as in the case of the disc, the conical mock-up was continued obliquely with a  $30^\circ$  tilted edge of 12 mm thickness. The spherical mock-up shown in figures 3(e) and 3(f) corresponds to a truncated hemispherical shell with an external radius of curvature of 353.6 mm and a thickness of 15 mm. In contrast to the other mock-ups, the spherical mock-up was continued tangentially by 40 mm. The extrapolated sides of each mock-up were covered with an aluminium cellotape because of the bad quality of the polishing in these regions. The cellotape acted as a light guide which increased the diffusion of light in the shell and limited the direct lighting of the free surface by the diffusive peripheral regions of the mock-ups. Note that in Tassin *et al.* (2017), it was not necessary to cover the periphery of the mock-up by aluminium cellotape thanks to the good quality of the polishing. The edge of the mock-ups in contact with the LEDs was roughened to homogenize the light diffusion in the material.

## 2.2. Compensation of optical distortion

In the case of the three-dimensional mock-ups (cone, sphere), it was necessary to compensate for the optical distortion due to the perspective effects (mainly). In order to do so, we manufactured calibration parts over which the projection of a regular grid was printed. These parts were placed in contact with the lower face of the mock-up (see figure 4) and an image of the grids seen through the mock-up was recorded with the video camera before the series of experiments (see figure 5a). The localization of the intersections between the vertical and horizontal lines in the calibration images was performed with an in-house algorithm developed for the detection of the intersections. A comparison of the measured and theoretical positions of the grid intersections in the case of the cone is shown in figure 5(b). The intersection-point positions were then used to identify an eighth-order polynomial correction model (see Tang *et al.* 2017) of the following form:

$$\begin{cases} x_2 = a_1x_1^8 + a_2x_1^7y_1 + \dots + a_{44}y_1 + a_{45} \\ y_2 = b_1x_1^8 + b_2x_1^7y_1 + \dots + b_{44}y_1 + b_{45} \end{cases} \quad (2.1)$$

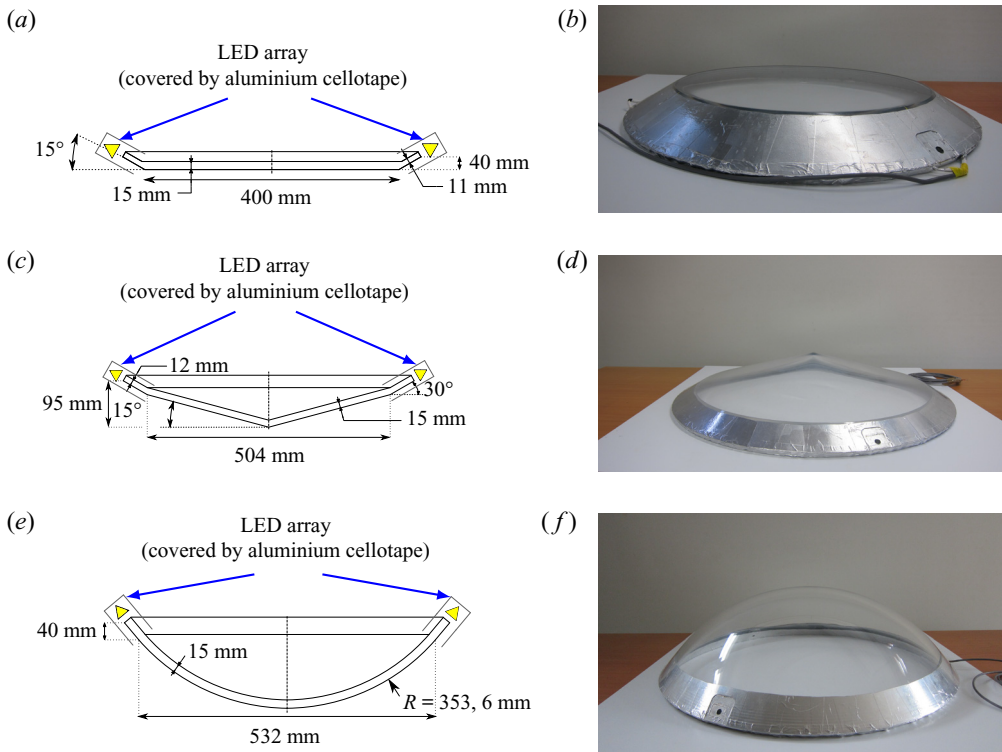


FIGURE 3. Description of the different mock-ups used in the experiments. (a) Description of the circular disc. (b) Photograph of the disc. (c) Description of the circular cone. (d) Photograph of the cone. (e) Description of the sphere. (f) Photograph of the sphere.

where  $(x_1, y_1)$  are the positions of the pixels as observed by the camera and  $(x_2, y_2)$  are the corrected positions of the points in the  $x$ - $y$  plane. The value of the parameters of the correction model  $(a_1, \dots, a_{45}, b_1, \dots, b_{45})$  were adjusted using an optimization algorithm based on the minimization of the distance between the measured and theoretical position of the calibration grid intersections. The absolute residual error maps after calibration for the cone and for the sphere are displayed in figures 5(c) and 5(d), respectively. One can see in figures 5(c) and 5(d) that the average residual error after calibration is lower than one millimetre, except near the centre of the cone where the error reaches 2 mm. The higher error near the centre of the cone can be explained by the presence of manufacturing imperfections at the centre of the cone which affect the accuracy of the intersection detection algorithm. We verified *a posteriori* that the distortion was negligible in the case of the circular disc (a calibration part was also manufactured for this mock-up).

### 2.3. Initial position of the mock-up

The adjustment of the initial position of the mock-ups in terms of altitude and horizontality is an important feature of the experimental methodology. Different approaches were used for the flat mock-up (circular disc) and the three-dimensional mock-ups (cone and sphere). In the case of the circular disc, the horizontality of the mock-up was first adjusted using an inclinometer (0.05° resolution) laying on the upper surface of the mock-up. Then the mock-up was lowered vertically step by step until it touched the still water. The mock-up

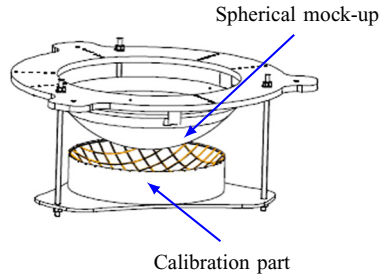


FIGURE 4. Calibration part manufactured for the sphere.

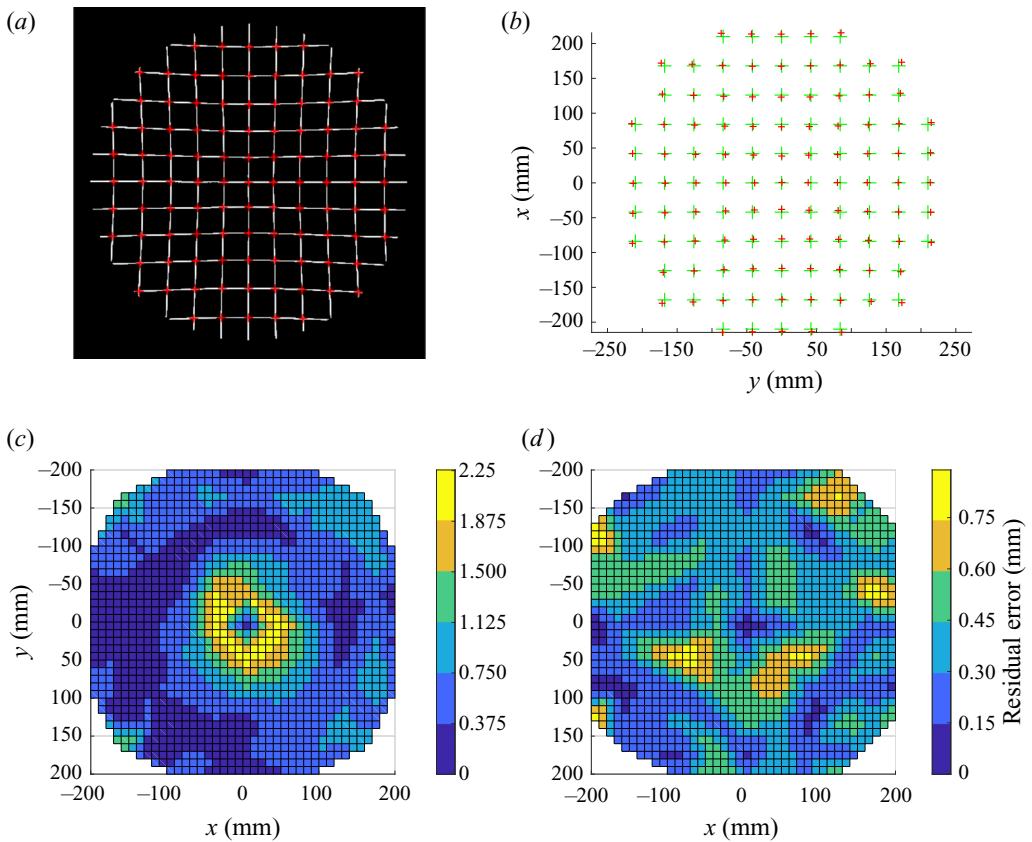


FIGURE 5. Compensation of optical distortion method. (a) Calibration grid seen through the cone with reversed contrast. (b) Comparison between the theoretical position of the intersections (large green crosses) and the detected crosses (small red crosses) from panel (a). (c) Residual error after calibration of the cone. (d) Residual error after calibration of the sphere.

became fully wetted within a final step of 0.5 mm. This final position was used as the initial position for all the water exit experiments carried out with the circular disc. Note, however, that the initial radius of the wetted surface was greater than the flat part of the mock-up because of the presence of a meniscus wetting a portion of the sloped part of the mock-up (see figure 6a).



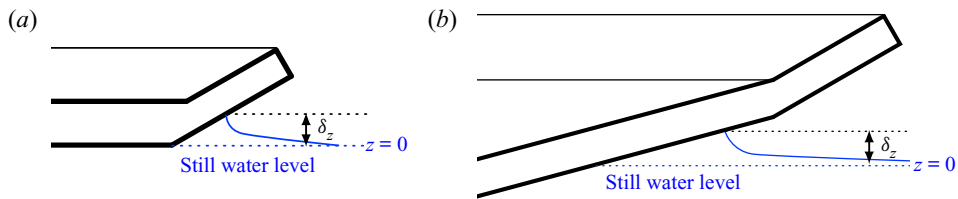


FIGURE 6. Illustration of the meniscus. (a) Circular mock-up. (b) Conical mock-up.

A different approach was used for the adjustment of the ‘horizontality’ of the three-dimensional mock-ups due to the absence of a horizontal plane surface to place the inclinometer. In this case, the mock-up was first partially wetted and then the horizontality was adjusted in order to obtain a symmetric wetted surface (for this purpose, an image of the calibration grid was superimposed to the image of the camera). Finally, the vertical position of the mock-up was adjusted to obtain the desired value of the wetted surface radius. This position was used as the reference position in the water exit and entry–exit experiments. Note that, with this methodology, the size of the wetted surface is influenced by the presence of the meniscus. This means that the boundary of the wetted surface does not correspond to the intersection of the still water surface with the lower surface of the mock-up (see figure 6*b*).

#### 2.4. Motion prescribed to the mock-up

In the water exit experiments, the elevation of the mock-up,  $h(t)$ , with respect to its initial position follows the following time evolution:

$$\begin{cases} h(t) = H[1 + \operatorname{erf}(U_{\max}(t - t_0)\sqrt{\pi}/H)]/2, & t \leq t_0, \\ \dot{h}(t) = U_{\max}, & t \geq t_0, \end{cases} \quad (2.2)$$

with  $\operatorname{erf}(x) = (2/\sqrt{\pi}) \int_0^x \exp(-\tau^2) d\tau$  the error function,  $U_{\max}$  the maximum velocity reached during the experiment,  $H$  the maximum elevation of the mock-up and  $\dot{h}(t)$  the time derivative of  $h(t)$ . In the water exit experiments, the value of  $H$  was fixed to 10 cm, the value of  $U_{\max}$  was varied from 0.2 to 0.6  $\text{m s}^{-1}$  and  $t_0$  was set to 3 s. The time history of the velocity and acceleration for the different values of  $U_{\max}$  is illustrated in figure 7. Formally speaking,  $h(t)$  tends to 0 at  $t = -\infty$ , but in practice  $h(0)$  was considered to be sufficiently small to be neglected in the experiments. Note that this motion was inspired by Reis *et al.* (2010) who originally studied the water exit phenomenon in order to understand the cat lapping phenomenon. Following Reis *et al.* (2010), the characteristic speed  $U_{\max}$  and the initial wetted surface radius  $c_0$  can be used to calculate the Froude ( $Fr$ ), Reynolds ( $Re$ ) and Weber ( $We$ ) numbers for the water exit experiments:  $Fr = U_{\max}/\sqrt{gc_0}$ ,  $Re = U_{\max}c_0/\nu$  and  $We = \rho c_0 U_{\max}^2/\sigma$ , with  $g$  the acceleration due to gravity,  $\nu$  the liquid kinematic viscosity and  $\sigma$  the surface tension coefficient. In the water exit experiments, the value of  $Fr$  ranges from 0.13 ( $U_{\max} = 0.2 \text{ m s}^{-1}$ ,  $c_0 = 0.25 \text{ m}$ ) to 0.43 ( $U_{\max} = 0.6 \text{ m s}^{-1}$ ,  $c_0 = 0.2 \text{ m}$ ),  $Re \approx 4.0 \times 10^4$  to  $1.5 \times 10^5$  and  $We \approx 1.1 \times 10^2$  to  $1.2 \times 10^3$ .

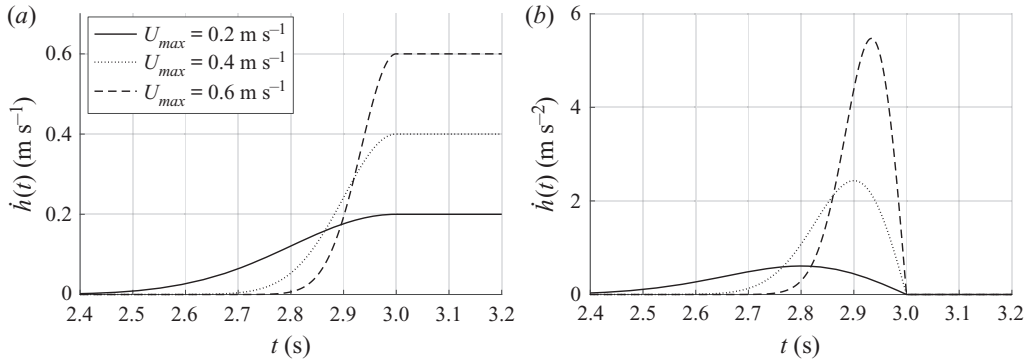


FIGURE 7. Evolution of the velocity (a) and acceleration (b) as a function of time during the water exit experiments for different values of  $U_{max}$ .

In the water entry and exit experiments, the elevation of the lowest point of the mock-up,  $h(t)$ , with respect to the free-surface altitude follows the following time evolution:

$$\begin{cases} h(t) = -(H/2) \cdot \text{erf}(U_{max}(t - t_0)\sqrt{\pi}/H), & t \leq t_0, \\ h(t) = -H \sin(2\pi(t - t_0)/T), & t_0 \leq t \leq T/2 + t_0, \\ \dot{h}(t) = U_{max}, & t \geq T/2 + t_0 \end{cases} \quad (2.3)$$

with  $U_{max}$  the maximum velocity and  $T = 2\pi H/U_{max}$ ;  $H$  is the maximum submergence depth and  $t_0 = 3$  s. The body enters the water at  $t_0$  with an initial velocity equal to  $-U_{max}$ . The acceleration is maximum at  $t = T/4 + t_0$  when the body begins to move upward. Note that for  $t \leq t_0$ , the motion prescribed to accelerate the mock-up to the desired entry velocity follows the same evolution as for the exit experiments, but in the downward direction. Using the axisymmetric formulation of Wagner’s theory,  $H$  can be related to  $c_{max}$ , the maximum wetted surface radius expected to be reached in an experiment. For the  $15^\circ$  cone, the Wagner condition (see Korobkin & Socolan 2006, equation (48)) reads:  $H = \pi \tan(15^\circ)c_{max}/4$  and for the sphere:  $H = \int_0^{\pi/2} \sin \beta [R - \sqrt{R^2 - c_{max}^2 \sin^2 \beta}] d\beta$ , where  $R = 353.6$  mm. The values of the maximum acceleration attained during the different combined entry and exit experiments are reported in table 1. The Froude, Reynolds and Weber numbers can be calculated in a similar way as for the exit experiments, except that  $c_0$  should be replaced by  $c_{max}$ . The values of  $Fr$  corresponding to the experiments are given in table 1.

### 3. Method of experimental analysis

In this section we describe the method used to analyse the results obtained from the different experiments.

#### 3.1. Synchronization of the measurements with the motion generator

The data acquisition system and the high-speed video camera were triggered by the same signal coming from the motion generator, and so were well synchronized to each other with a maximum time shift of 1 ms (the sampling frequency and frame rate were both set to 1 kHz). However, it was not possible to accurately synchronize the motion

Cone				Sphere			
$c_{max}$ (mm)	$U_{max}$ (m s <sup>-1</sup> )	max( $\ddot{h}$ ) (m s <sup>-2</sup> )	$Fr$	$c_{max}$ (mm)	$U_{max}$ (m s <sup>-1</sup> )	max( $\ddot{h}$ ) (m s <sup>-2</sup> )	$Fr$
200	0.57	7.72	0.41	200	0.56	7.74	0.40
200	0.4	3.80	0.29	200	0.4	3.95	0.29
250	0.6	6.84	0.38	250	0.6	5.41	0.38
250	0.4	3.04	0.26				

TABLE 1. Froude number and maximum acceleration attained during the combined entry and exit experiments for the different values of  $c_{max}$  and  $U_{max}$ .

of the hexapod and the data/video acquisition system during the experiments. In our analysis of the experiments, we compared the theoretical acceleration evolution and the recorded acceleration signal to ‘re-synchronize’ the measurements with the motion. The time shift between the motion and the measured signals was obtained by maximizing the cross-correlation between the measured and theoretical acceleration signals. In order to do so, we filtered the high-frequency oscillations of the measured acceleration signals using a Fourier low-pass filter with a cutoff frequency of 30 Hz. An example of the raw and filtered acceleration signals measured during a water exit experiment with  $U_{max} = 0.6 \text{ m s}^{-1}$  is depicted in figure 8. A comparison of the theoretical and measured acceleration signals is presented in figure 9. The theoretical acceleration signal after applying the same low-pass filter is also depicted in figure 9 to show that the filtering operation does not affect the dynamics of the motion. We can see that the hexapod follows quite well the target motion even if the measured acceleration exhibits a small oscillation which leads to a difference of about  $0.28 \text{ m s}^{-2}$  in terms of the acceleration peak value. Despite the small oscillations of the acceleration signal, the motion of the hexapod is very repeatable as it can be seen in figure 10 where we compare the filtered acceleration signals recorded during three experiments of exit in air with  $U_{max} = 0.6 \text{ m s}^{-1}$ .

### 3.2. Tracking of the contact line

A sequence of four images recorded during the water entry and exit of the cone for different time instants is plotted in figure 11. During the entry stage (figures 11a and 11b), both the jet front and the contact line are clearly visible. Indeed, they are both illuminated by the LED edge-lighting system. During the exit stage (figures 11c and 11d), the jet disappears but the contact line, which contracts towards the centre, is still clearly visible. Some additional concentric luminous rings are nevertheless visible in figures 11(c) and 11(d). These features are imparted to undesired specular reflections of the very bright outer region of the mock-up on the free surface, but their presence does not alter the tracking of the contact line which corresponds to the inner luminous ring in the images. In order to measure the evolution of the contact line during the experiments, the contact line geometry is extracted using a contour detection algorithm based on the method of Taubin (1991) and assuming that the shape of the contact line is elliptic. The performance of the contour tracking algorithm is illustrated in figure 12 where the detected contours and the original images (from figure 11) are superimposed. The tracking of the contact line is not problematic, except for a very short duration at the moment of the transition between the entry stage and the exit stage because the contact line is not bright enough.

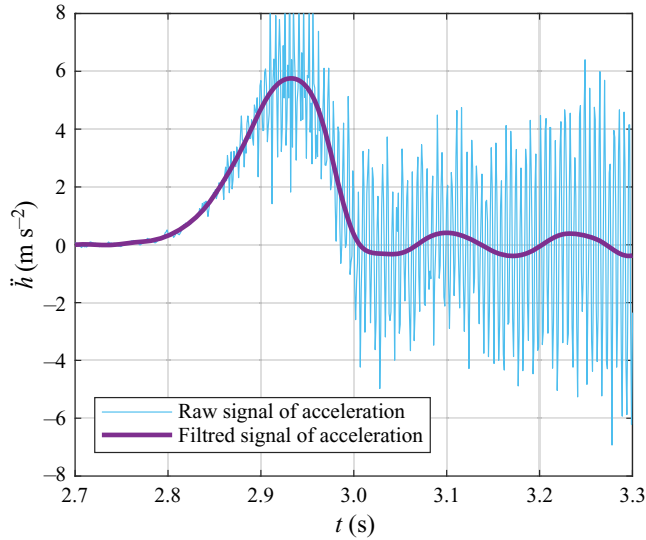


FIGURE 8. Comparison of the original and filtered measured acceleration signals during a water exit experiment with  $U_{max} = 0.6 \text{ m s}^{-1}$ .

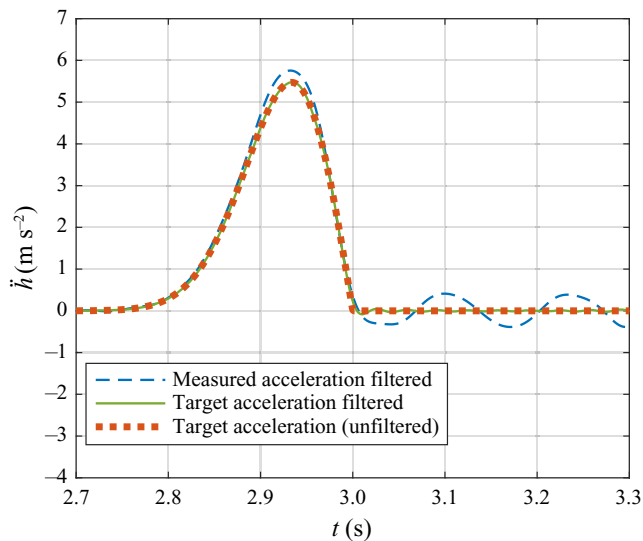


FIGURE 9. Comparison of the filtered measured and target acceleration (filtered and unfiltered) for water exit with  $U_{max} = 0.6 \text{ m s}^{-1}$ .

In order to verify that the inner ring corresponds to the contour of the wetted surface (the contact line), the same experiments were conducted with a draughtboard laying at the bottom of the tank (approximately 2 m below the free surface). With this technique, the region over which the water is in contact with the mock-up corresponds to the region over which the draughtboard appears undistorted (except for the optical distortion due to the shape of the mock-up), as shown in figure 13. The red dashed line, which is superimposed on the images obtained with the draughtboard technique in figure 13, corresponds to the contour extracted from figure 12. One can observe that the region over which the

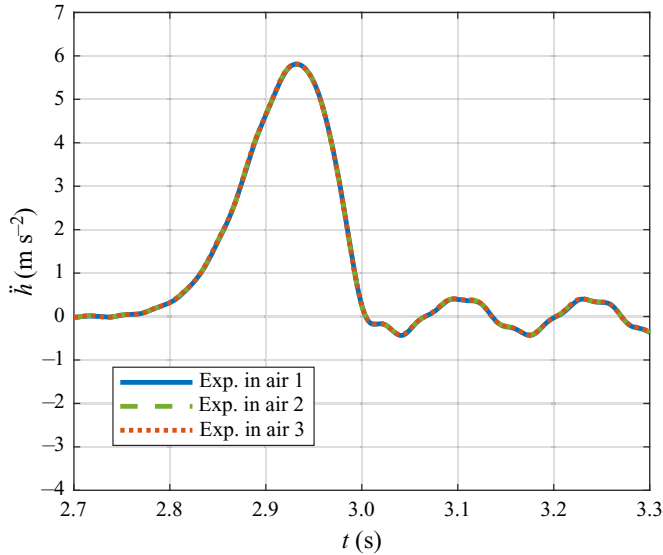


FIGURE 10. Comparison of the measured acceleration signals for three similar exit experiments in air with  $U_{max} = 0.6 \text{ m s}^{-1}$ .

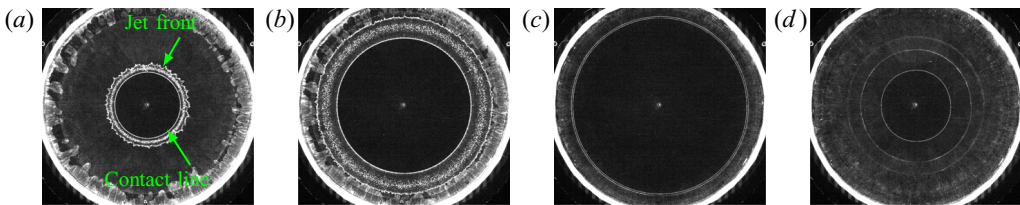


FIGURE 11. Sequence of images obtained during the water entry (*a,b*) and exit (*c,d*) of the cone with  $c_{max} = 250 \text{ mm}$  and  $U_{max} = 0.6 \text{ m s}^{-1}$ : (*a*)  $t = 3.036 \text{ s}$ , (*b*)  $t = 3.073 \text{ s}$ , (*c*)  $t = 3.166 \text{ s}$  and (*d*)  $t = 3.318 \text{ s}$ .

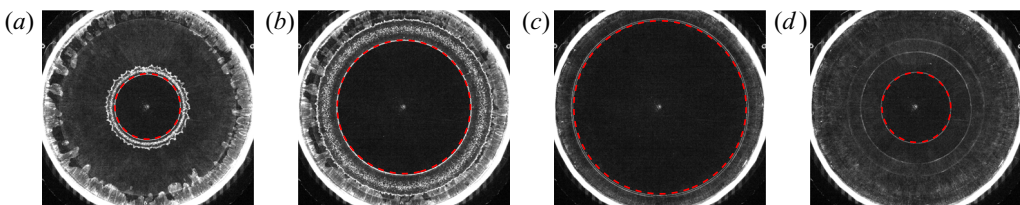


FIGURE 12. Tracking of the contact line during the water entry (*a,b*) and exit (*c,d*) of the cone: (*a*)  $t = 3.036 \text{ s}$ , (*b*)  $t = 3.073 \text{ s}$ , (*c*)  $t = 3.166 \text{ s}$  and (*d*)  $t = 3.318 \text{ s}$ .

draughtboard remains undistorted is perfectly circumscribed by the contour extracted from figure 12. This comparison demonstrates the accuracy of the LED edge-lighting technique for both water entry and water exit experiments. A more detailed validation of the LED edge-lighting technique through comparison with images obtained with the draughtboard technique for the different mock-ups is presented in appendix A.

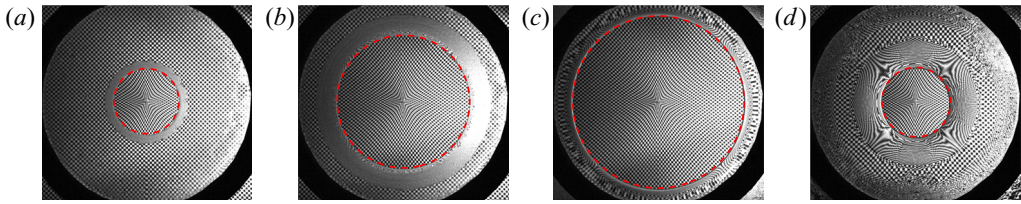


FIGURE 13. Comparison between the contact line obtained with the LED edge-lighting technique (red dashed line) and the images obtained with the draughtboard during the water entry and exit of the cone: (a)  $t = 3.036$  s, (b)  $t = 3.073$  s, (c)  $t = 3.166$  s and (d)  $t = 3.318$  s.

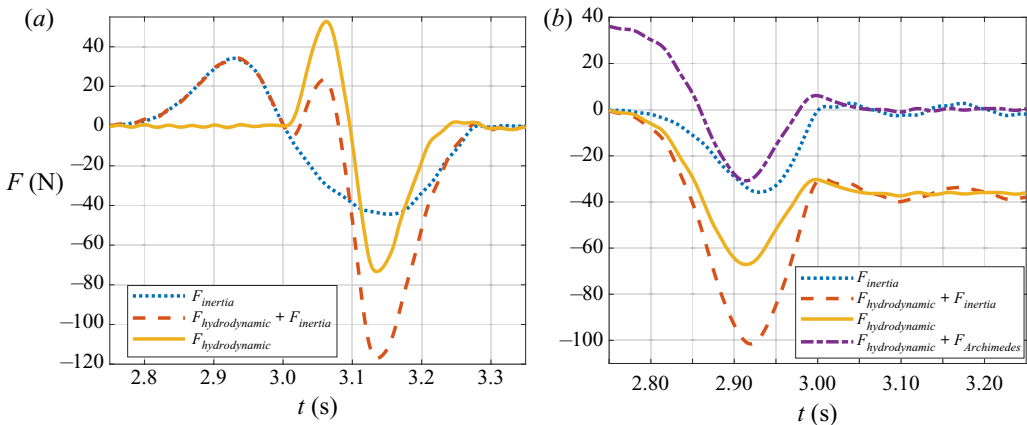


FIGURE 14. Contribution of the different force components to the total force. (a) Water entry and exit of a cone with  $U_{max} = 0.6$  m s<sup>-1</sup> and  $c_{max} = 250$  mm. (b) Water exit of a cone with  $U_{max} = 0.6$  m s<sup>-1</sup> and  $c_0 = 250$  mm.

### 3.3. Hydrodynamic force measurement

In our analysis procedure, the force signals are first low-pass filtered with the same filter as the acceleration signal. It was shown previously that the filtering operation did not affect the acceleration signal (see figure 9). Given that the hydrodynamic force during water exit is principally due to an ‘added mass-like’ effect (see Tassin *et al.* 2012; Korobkin 2013), we can anticipate that the filtering will not affect the force signals (except for the removal of the high-frequency oscillations). The force measured by the sensors is a combination of the action of the water on the mock-up and the inertia force due to the mass of the mock-up and of the mechanical parts connecting the mock-up to the force sensors. In order to subtract the force component due to inertia from the total measured force, the inertia component was measured by running experiments in air with a motion identical to the experiments with water. Each experiment in air and water was repeated three times with the same prescribed motion. The measured total force and the contribution of the different force components during an experiment of water entry and exit with the cone are plotted in figure 14(a). One can appreciate the relative importance of the inertia component ( $F_{inertia}$ ) to the total force.

The use of piezoelectric force sensors, even with a slow-drift charge amplifier like the one we used, requires a reset of the level of reference of the force sensors at the beginning of the experiment. As a consequence, the measured hydrodynamic force is equal to zero at the beginning of the pure exit experiment, even for the three-dimensional mock-ups,

$c_0$ (mm)	$U_{max}$ (m s <sup>-1</sup> )	$\delta_t$ (s)	$ h(t_0 + \delta_t) $ (mm)	$\delta_z^*$ (mm)
250	0.6	0.005	3.0	3.6
200	0.57	0.0048	2.8	3.8

TABLE 2. Estimation of the meniscus height  $\delta_z$  for the cone:  $\delta_z^*$  is the estimate of  $\delta_z$  based on the measured value of Archimedes' force and  $|h(t_0 + \delta_t)|$  is the estimate of  $\delta_z$  based on the measured value of  $\delta_t$ .

$c_0$ (mm)	$U_{max}$ (m s <sup>-1</sup> )	$\delta_t$ (s)	$ h(t_0 + \delta_t) $ (mm)	$\delta_z^*$ (mm)
250	0.6	0.008	4.8	4.3
200	0.56	0.007	3.9	4.2

TABLE 3. Estimation of the meniscus height  $\delta_z$  for the sphere:  $\delta_z^*$  is the estimate of  $\delta_z$  based on the measured value of Archimedes' force and  $|h(t_0 + \delta_t)|$  is the estimate of  $\delta_z$  based on the measured value of  $\delta_t$ .

despite the action of Archimedes' force. In the results presented in the following sections, the reset of the force sensors is corrected by subtracting the final asymptotic value of the hydrodynamic force (when the mock-up is fully unwetted and the velocity is null). The contribution of the different force components during the water exit of the cone are shown in [figure 14\(b\)](#).

### 3.4. Correction of the reference elevation in the water entry and exit experiments

The presence of the meniscus induces an uncertainty of  $\delta_z$  (corresponding to the meniscus height) on the initial position of the three-dimensional mock-ups (with respect to the still water level). However, the height of the meniscus can be estimated from the experiments in two ways. The first way is to find a value of  $\delta_z$  such that the theoretical buoyancy force is equal to the measured force at the beginning of the water exit experiment. The second way is to detect from the high-speed videos the time instant when the mock-up touches the water ( $t = t_0 + \delta_t$ ) and to compute the theoretical elevation of the mock-up at this time instant ( $h(t_0 + \delta_t)$ ). The values obtained for  $\delta_z$  with the two approaches for the cone and the sphere are given in [tables 2](#) and [3](#), respectively. One can see that the maximum difference between the two estimates is about 1 mm. Note that these values will be used later in order to make comparisons with the theoretical results.

## 4. Experimental results

In this section we present the experimental results in terms of the evolution of the radius of the wetted surface and of the hydrodynamic force measured during the experiments of pure water exit (§ 4.1) and combined water entry and exit (§§ 4.2 and 4.3).

### 4.1. Evolution of the wetted surface and of the hydrodynamic force during the water exit experiments

The evolution of the radius of the wetted surface during the water exit of the circular disc is depicted in [figure 15](#) for different values of the maximum exit velocity. The corresponding

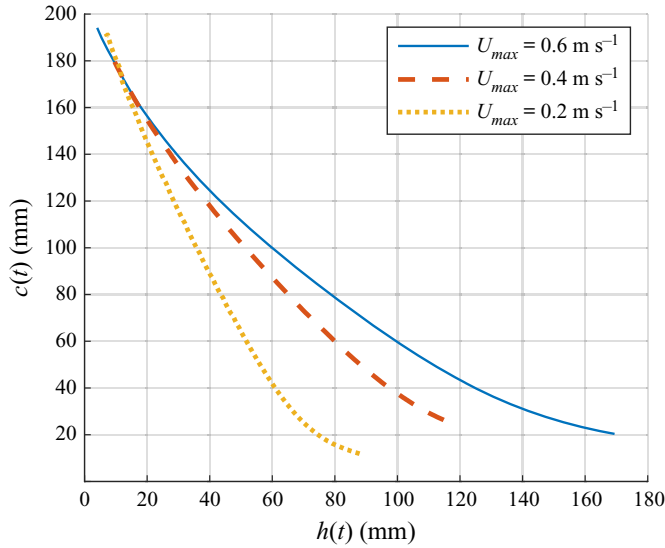


FIGURE 15. Evolution of the radius of the wetted surface as a function of the elevation during the water exit of the circular disc for different values of  $U_{max}$ .

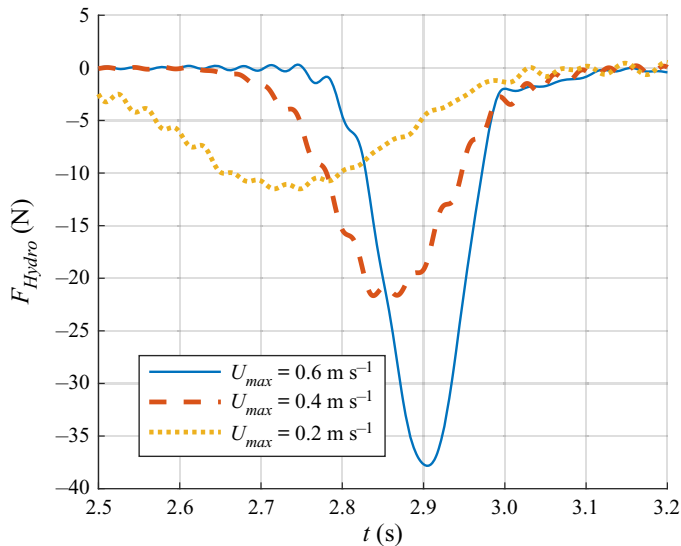


FIGURE 16. Evolution of the hydrodynamic force as a function of time during the water exit of the circular disc for different values of  $U_{max}$ .

force evolutions are presented in figure 16. One can observe in figure 15 that the evolution of the wetted surface radius depends on the exit velocity. For a given disc elevation, the radius is smaller when the velocity is decreased. This phenomenon is due to the action of the gravity. As the maximum exit velocity decreases, the peak (absolute) value of the hydrodynamic force decreases and occurs earlier.

The results obtained with the cone are depicted in figures 17 and 18. Similarly to the circular disc, the reduction of the wetted surface radius with the elevation is more



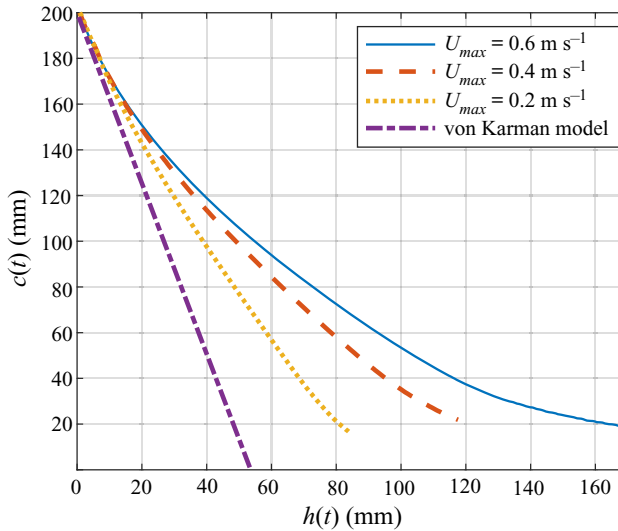


FIGURE 17. Evolution of the radius of the wetted surface as a function of the elevation during the water exit of the cone for different values of  $U_{max}$ .

pronounced as the velocity decreases. In figure 17, the evolution of the radius of the wetted surface obtained with a von Karman approach is also plotted. Within the von Karman approach, the contact line position is determined as the intersection between the body surface and the reference horizontal plane  $z = \delta_z$  (represented by a black dotted line in figure 6b). The difference between the experimental results and the results obtained with the von Karman approach illustrates the pile-up of the free surface induced by the water exit. The hydrodynamic force evolutions measured during the water exit of the cone differ from that measured during the water exit of the circular disc due to the static buoyancy of the cone. The buoyancy force mitigates the suction force in the case of the cone. For the lowest velocity ( $U_{max} = 0.2 \text{ m s}^{-1}$ ), the hydrodynamic force remains positive during the entire duration of the exit experiment. In agreement with what can be expected from a theoretical model of exit based on an added mass approach, the hydrodynamic force measured during the water exit of the disc and the cone becomes very low when the acceleration vanishes (at  $t = 3 \text{ s}$ ). However, it is not equal to zero. Indeed, a drag force is observed for  $t > 3 \text{ s}$ . This force decreases gradually with time, most likely because of the decrease of the size of the wetted surface.

The results obtained during the water exit of the sphere are presented in figures 19 and 20. In this case, the velocity has a much smaller influence on the evolution of the radius of the wetted surface. One may expect that the effect of the gravity would be more pronounced in the case of the sphere due to the larger volume displaced by the mock-up, but the difference between the experimental results and the results obtained with the von Karman approach (also plotted in figure 19) demonstrates that the phenomenon is not quasi-static. Also note that the hydrodynamic force remains positive during almost the entire duration of the experiments, even for the highest maximum velocity ( $0.6 \text{ m s}^{-1}$ ), due to the importance of the buoyancy force.

#### 4.2. Water entry and exit of the cone

The evolutions of the radius of the wetted surface during the combined water entry and exit of the cone are presented in figures 21 and 22 for  $c_{max} = 200 \text{ mm}$  and  $c_{max} = 250 \text{ mm}$ , respectively. The maximum radius,  $c_{max}$ , corresponds to the theoretical value of the radius

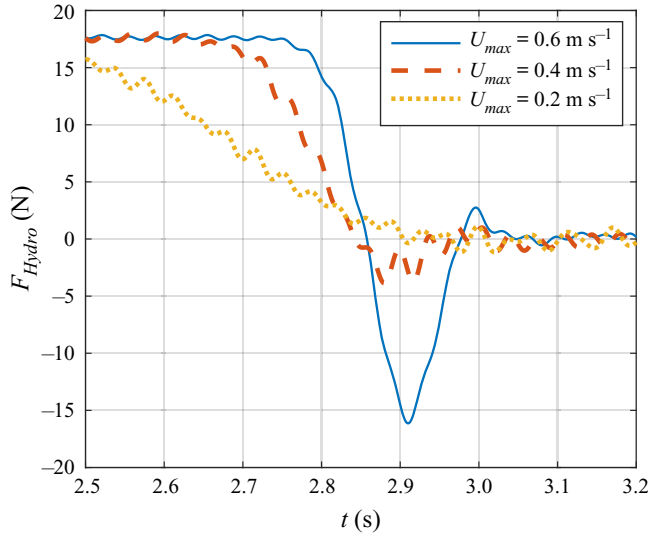


FIGURE 18. Evolution of the hydrodynamic force as a function of time during the water exit of the cone for different values of  $U_{max}$ .

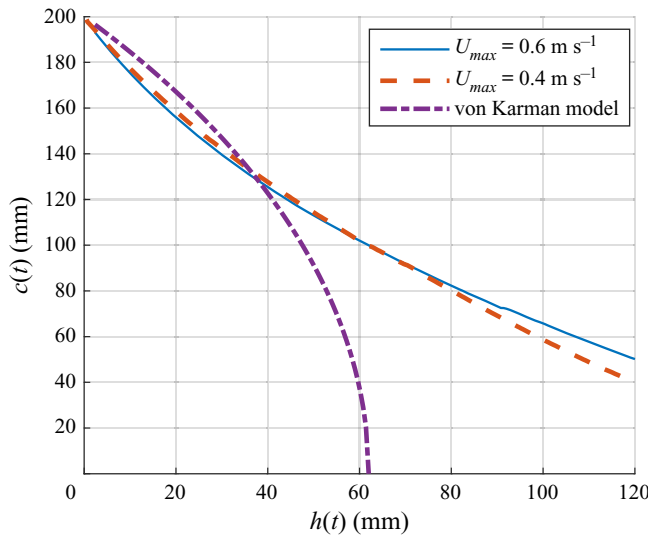


FIGURE 19. Evolution of the radius of the wetted surface as a function of the elevation during the water exit of the sphere for different values of  $U_{max}$ .

of the wetted surface obtained with the Wagner model when the penetration depth is maximum (at  $t = t_0 + T/4$ ). Note that the maximum value of  $c_{max}$  is not attained during the experiments. We will see later that this can be explained by a value of  $\delta_z \approx 3$  mm. The value of the maximum velocity ( $U_{max}$ ) has little effect on the maximum value of the radius of the wetted surface. This indicates that gravity does not affect the wetted surface evolution during the entry stage (for the considered entry velocities). The evolution of the hydrodynamic force for  $c_{max} = 200$  mm and for  $c_{max} = 250$  mm is shown in [figures 23](#)

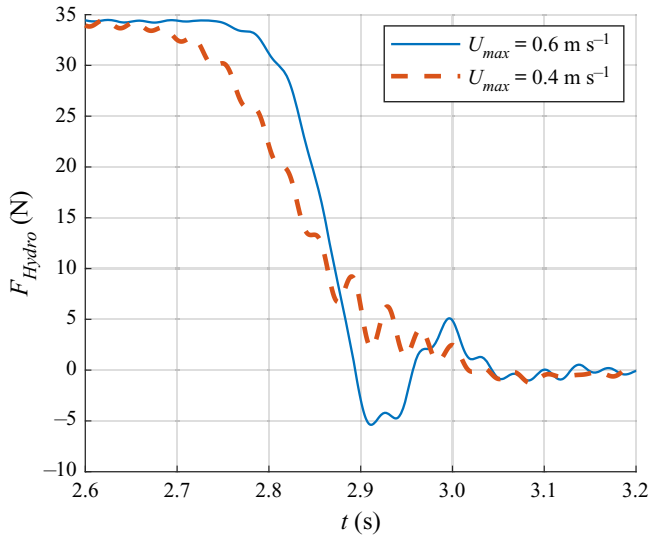


FIGURE 20. Evolution of the hydrodynamic force as a function of time during the water exit of the sphere for different values of  $U_{max}$ .

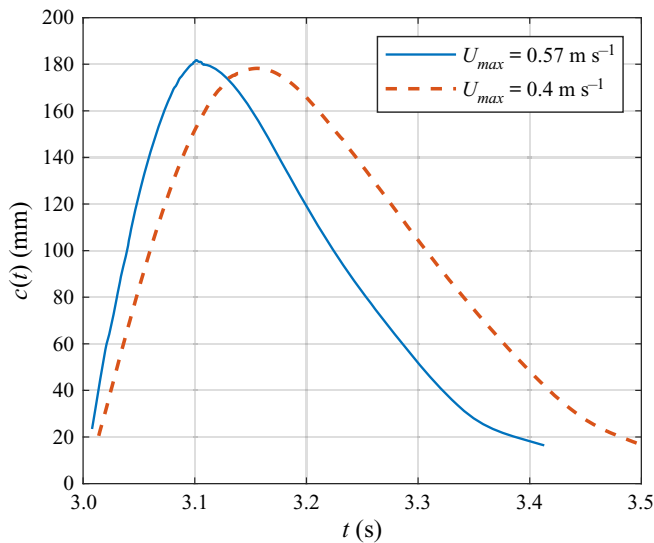


FIGURE 21. Evolution of the radius of the contact line as a function of time during the water entry and exit of the cone for  $c_{max} = 200$  mm.

and 24, respectively. According to the image recordings, the cone starts touching the water at  $t = t_0 + \delta_t \approx 3.005$  s (see table 2). After that, the load begins to increase and reaches rapidly a maximum. Then, the load decreases and becomes negative (corresponding to suction forces). It should be noted that at the time when the force is equal to zero, the mock-up velocity is still downward. The duration of the stage during which the force is negative is longer than the one during which it is positive. In addition, the maximum force, in terms of magnitude, corresponds to a suction load (directed downward) and is reached at the transition between the entry and exit stages. This observation is in line

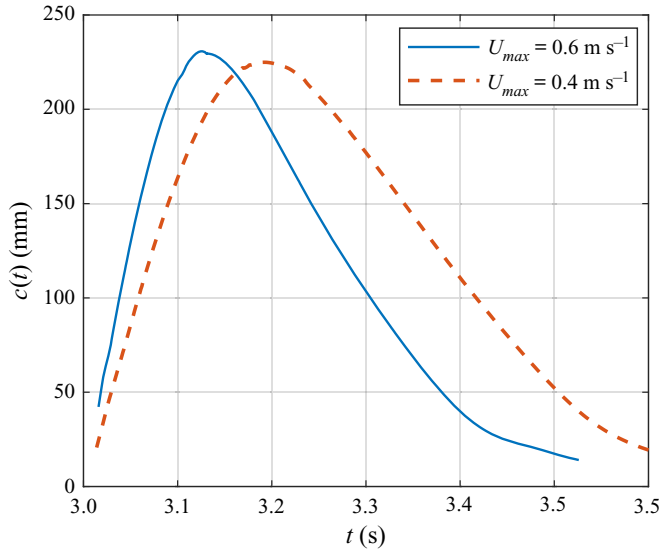


FIGURE 22. Evolution of the radius of the contact line as a function of time during the water entry and exit of the cone for  $c_{max} = 250$  mm.

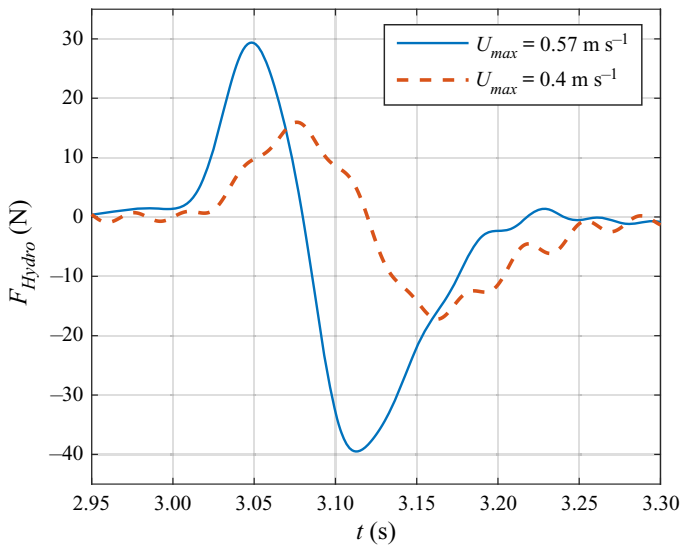


FIGURE 23. Evolution of the hydrodynamic force as a function of time during the water entry and exit of the cone for  $c_{max} = 200$  mm.

with the experimental observations and theoretical predictions of Baarholm & Faltinsen (2004) and Tassin *et al.* (2013). Note that the force results measured during the experiments with  $U_{max} = 0.4$  m s<sup>-1</sup> exhibit more oscillations than the results obtained with  $U_{max} = 0.57$  m s<sup>-1</sup>.

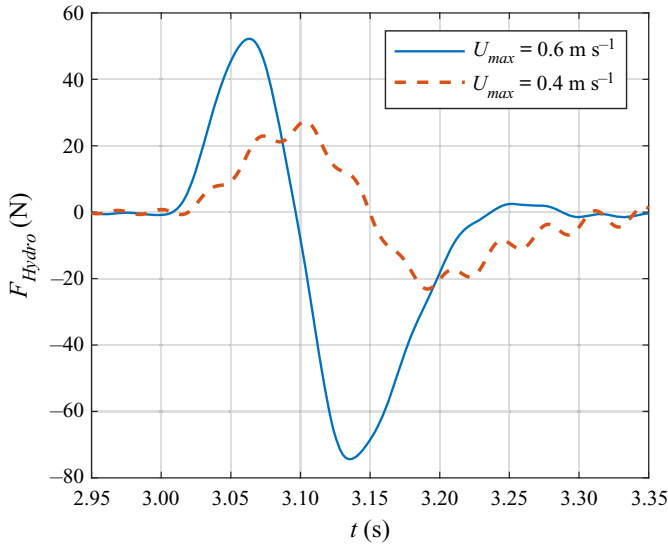


FIGURE 24. Evolution of the hydrodynamic force as a function of time during the water entry and exit of the cone for  $c_{max} = 250$  mm.

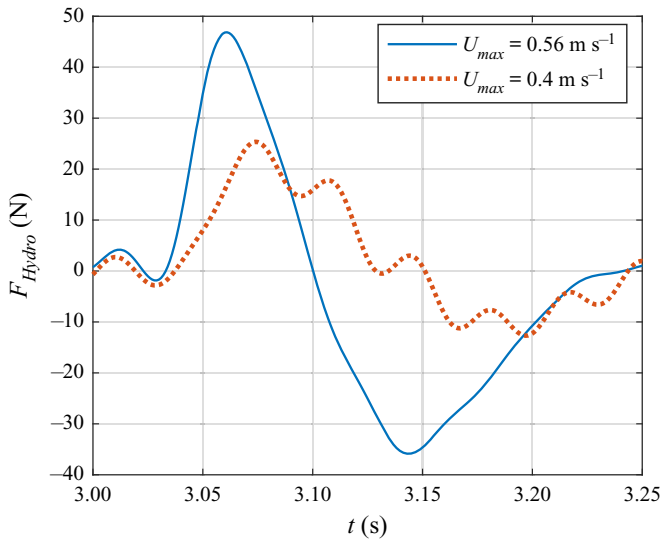


FIGURE 25. Evolution of the hydrodynamic force as a function of time during the water entry and exit of the sphere for two different velocities and a theoretical  $c_{max} = 200$  mm.

#### 4.3. Water entry and exit of the sphere

The evolution of the hydrodynamic force during the combined water entry and exit of the sphere is presented in figures 25 and 26 for  $c_{max} = 200$  mm and  $c_{max} = 250$  mm, respectively. Note that the cutoff frequency was set to 25 Hz instead of 30 Hz for the results presented in figure 26 in order to reduce the oscillations of the force signal due to the vibrations of the set-up. One can observe that, in contrast to the water entry and exit of the cone, the maximum magnitude of the force is more important during the entry stage than

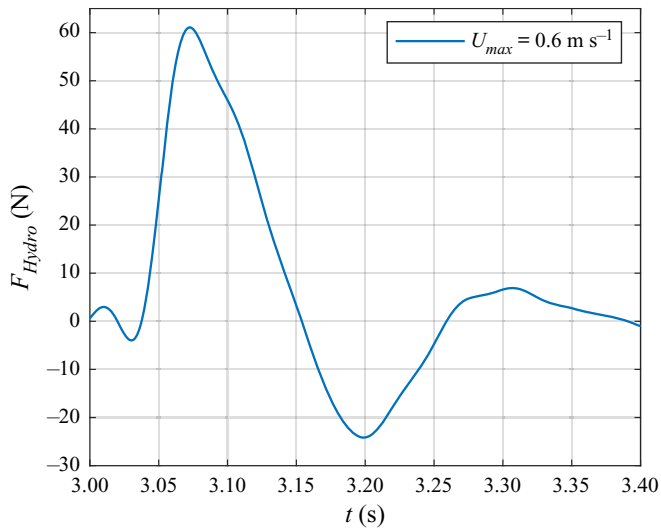


FIGURE 26. Evolution of the hydrodynamic force as a function of time during the water entry and exit of the sphere for a theoretical  $c_{max} = 250$  mm.

during the exit stage. Due to a weak contrast in the images, it has not been possible to use the automatic contact line tracking algorithm for the entry and exit experiments carried out with the sphere.

## 5. Investigation of different parameters affecting the water exit phenomenon and comparisons with theoretical results

In this section we investigate the effect of different parameters that influence the water exit phenomenon. We study the effect of the scale, the effect of the shape of the mock-up and the impact of the entry stage on the results of the exit stage. We also compare the measurements with theoretical results.

### 5.1. Effect of the scale (experiments in Froude similarity)

At present, there are still some open questions regarding the mechanisms governing the wetted surface dynamics in water exit problems. In particular, the question of the effect of surface tension and viscosity at the early stage of a water exit event was raised by Korobkin (2013). In order to assess the importance of these effects in our experiments, we conducted experiments in Froude similarity with the cone for different values of the initial wetted surface, hence varying the scale of the experiments (so varying the Reynolds and Weber numbers) while keeping the Froude number constant. The initial value of the radius of the wetted surface was varied from  $c_0 = 250$  mm to  $c_0 = 100$  mm. The scaling was based on a reference maximum velocity  $U_{max} = 0.6$  m s<sup>-1</sup>, a maximum elevation height  $H = 0.1$  m and  $c_0 = 0.25$  m. Assuming that  $\alpha = c_0/0.25$  (with the value of  $c_0$  in metres) represents the scale of the experiment, the function  $h(t)$  defining the motion of the cone for the different values of  $c_0$  is given by (2.2), with  $H = \alpha \times 0.1$  m,  $U_{max} = \sqrt{\alpha} \times 0.6$  m s<sup>-1</sup> and  $t_0 = \sqrt{\alpha} \times 3$  s. The results obtained for the different values of  $c_0$  are compared in figure 27 in terms of the non-dimensional radius of the wetted surface as a function of the non-dimensional elevation. One can see that the results obtained at different scales

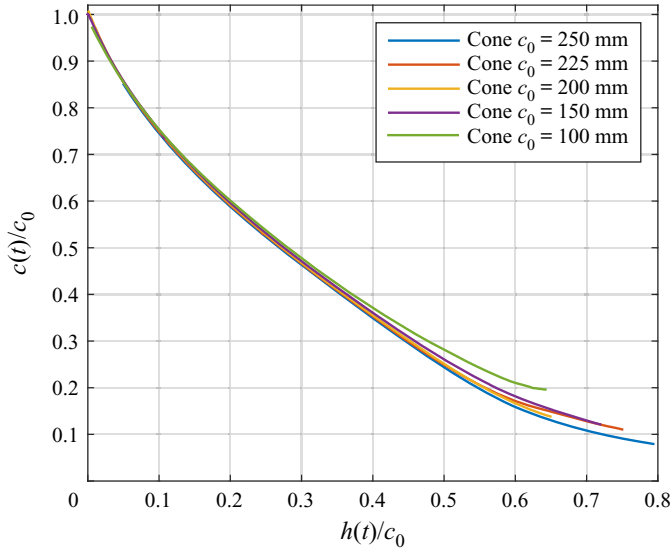


FIGURE 27. Evolution of the non-dimensional radius of the wetted area  $c(t)/c_0$  as a function of the non-dimensional elevation during the water exit of the cone for different values of  $c_0$  in Froude similarity.

are in very close agreement. Note, however, that the results obtained with  $c_0 = 100$  mm slightly deviate from the others at the end of the exit, but this difference remains within the accuracy margin of the experimental approach because of the imperfections at the centre of the conical mock-up (see figure 5c). These experiments show that the influence of surface tension and viscosity is marginal at the largest scales and that the dynamics of the wetted surface is mainly controlled by inertia and gravity effects. Following the theoretical work of Korobkin *et al.* (2017b) who showed that the quantity  $1 - c(t)/c_0$  was proportional to  $[h(t)/c_0]^{2/3}$  during the water exit of a flat plate at constant acceleration, the experimental results obtained in Froude similarity are depicted in figure 28 in terms of the quantity  $1 - c(t)/c_0$ . One can see that the results compare very well with the power law predicted by Korobkin *et al.* (2017b) (but with a different coefficient) for  $h(t)/c_0$  ranging from 0.1 to 0.7. This agreement is somewhat surprising given the influence of gravity in our experiments (see figure 17) and the rather different motion imposed to the cone.

### 5.2. Effect of the exit velocity

In this section, the effect of the exit velocity ( $U_{max}$ ) on the evolution of the contact surface during the water exit experiments is analysed by plotting the quantity  $1 - c(t)/c_0$  as a function of the non-dimensional elevation  $h(t)/c_0$ . The results obtained for the disc, the cone and the sphere are plotted in figures 29, 30 and 31, respectively. The experimental results of Vega-Martínez *et al.* (2019) corresponding to the water exit of an elastic circular disc are also shown for comparison in figure 29, but note that their experimental results are limited to  $c(t)/c_0 > 0.9$ . Two important conclusions can be drawn from these observations. First, the time history of the velocity (for  $U_{max}$  sufficiently large), the elasticity and the shape of the body do not seem to affect significantly the evolution of the radius of the wetted surface with the body elevation. Second, the theoretical prediction of Korobkin *et al.* (2017b), which is based on a self-similar small-time expansion,

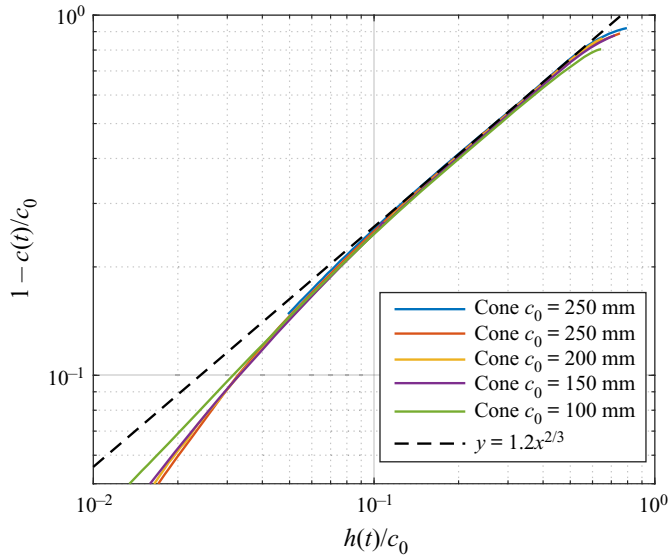


FIGURE 28. Evolution of  $1 - c(t)/c_0$  as a function of the non-dimensional elevation during the water exit of the cone for different values of  $c_0$  in Froude similarity with a log–log scale.

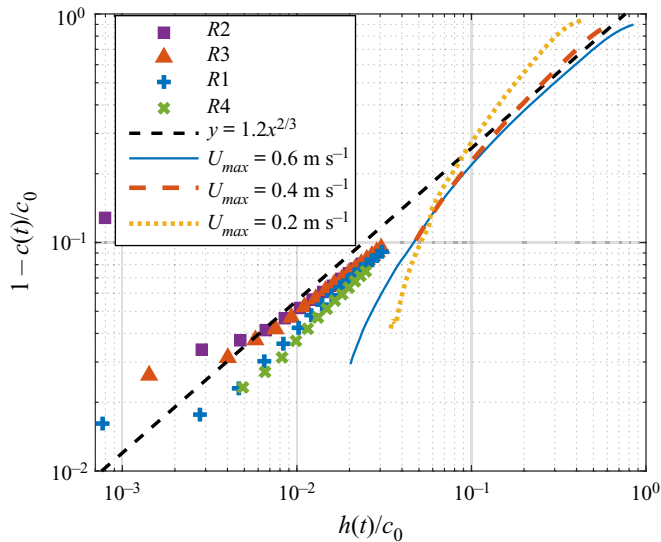


FIGURE 29. Evolution of  $[1 - c(t)/c_0]$  as a function of the non-dimensional elevation during the water exit of the disc for different values of  $U_{max}$ . The plots denoted by R1, R2, R3 and R4 correspond to four experimental results obtained by Vega-Martínez *et al.* (2019) with a 10.8 cm radius circular disc.

seems to be valid for values of  $h(t)/c_0$  as large as 0.7. However, as the value of  $U_{max}$  decreases, the power coefficient evolves. This effect, clearly visible for  $U_{max} = 0.2 \text{ m s}^{-1}$  in figures 29 and 30, is due to the influence of gravity.



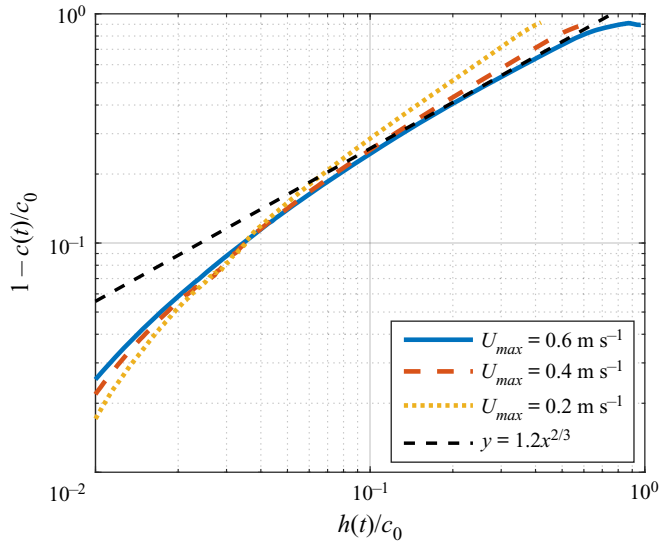


FIGURE 30. Evolution of  $[1 - c(t)/c_0]$  as a function of the non-dimensional elevation during the water exit of the cone for different values of  $U_{max}$ .

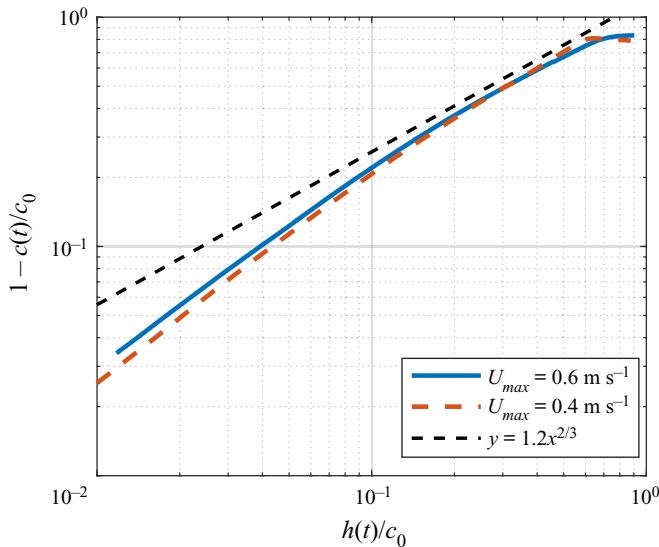


FIGURE 31. Evolution of  $[1 - c(t)/c_0]$  as a function of the non-dimensional elevation during the water exit of the sphere for different values of  $U_{max}$ .

### 5.3. Effect of the body shape

In the linearized water exit model proposed by Korobkin (2013), and further developed in Korobkin *et al.* (2017a), the body shape has no effect on the evolution of the wetted surface, provided that the size of the initial wetted surface and the body motion are similar. In order to confirm experimentally this assumption, we compare the results obtained with the different body shapes (circular disc, cone, sphere), but with a similar value of  $c_0$  and

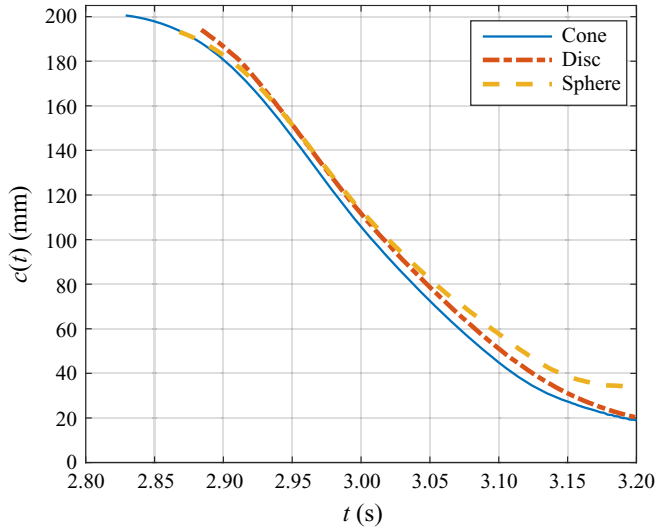


FIGURE 32. Effect of the body shape on the evolution of the radius of the wetted area  $c(t)$  during water exit experiments ( $U_{max} = 0.6 \text{ m s}^{-1}$  and  $c_0 = 200 \text{ mm}$ ).

a similar motion. Figure 32 shows the evolution of the radius of the wetted surface as a function of the elevation  $h(t)$  measured during the water exit of the three mock-ups for  $c_0 = 200 \text{ mm}$ . One can see that the evolution of the radius of the wetted surface for the cone and the disc are very close, except that the dewetting of the disc is delayed by a small time shift. This time shift may come from the fact that the initial radius of the wetted surface is slightly larger than 200 mm because of the meniscus. The evolution of the sphere seems to follow the evolution of the cone at the beginning of the experiments and then approaches the evolution of the disc. This comparison shows that the body shape has a marginal effect on the evolution of the wetted surface during water exit. This observation is consistent with the water exit model of Korobkin (2013) which is insensitive to the shape of the body exiting water (except for the size of the initial wetted surface). The hydrodynamic force measured during the experiments with the different body shapes is shown in figure 33. The total hydrodynamic force measured with the different mock-ups is largely affected by the importance of Archimedes' force. The results obtained after subtracting the initial value of the force are also depicted in figure 33 in order to compare the 'purely dynamic' contribution with the total hydrodynamic force in the different cases. This comparison shows that the dynamic contribution is rather close for the three shapes at the beginning of the exit (until  $t \approx 2, 9 \text{ s}$ ).

#### 5.4. Effect of the entry stage on the results of the exit stage

In the case of a combined water entry and exit event, the fluid is set in motion and the water free surface is deformed during the entry stage, and one may ask if the exit stage (when it takes place after an entry stage) may differ from a pure water exit experiment. In order to assess the effect of the entry stage on the exit stage, we compare the evolution of the wetted surface during an experiment of pure water exit (for  $U_{max} = 0.6 \text{ m s}^{-1}$ ) and during the exit stage of an experiment of combined water entry and exit (for  $U_{max} = 0.57 \text{ m s}^{-1}$ ) using the conical mock-up. We can see in figure 34 that, even if the dynamics of the mock-up is not exactly the same in both cases, the evolution of the radius of the wetted

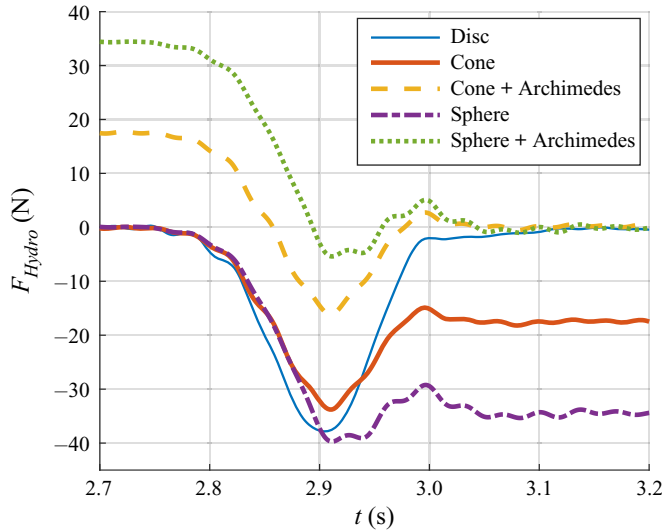


FIGURE 33. Effect of the body shape on the evolution of the hydrodynamic force  $F_{hydro}$  during water exit experiments ( $U_{max} = 0.6 \text{ m s}^{-1}$  and  $c_0 = 200 \text{ mm}$ ).

surface in the pure-exit experiment is comparable with that observed during the exit stage of a combined water entry and exit experiment. Note that the radius of the wetted surface measured during the combined water entry and exit experiments is non-dimensionalized with respect to the maximum value measured during the experiment. The same results are plotted in logarithmic scale in [figure 35](#). One can observe the very close agreement between the results measured during the exit stage of the combined water entry and exit experiment and the power law predicted by the theory of [Korobkin \*et al.\* \(2017b\)](#). These observations lead us to the important conclusion that a similar water exit model can be used to model both a pure water exit event and the exit stage of a combined water entry and exit event (e.g. in a  $2D + t$  approach such as the one used in [Bensch \*et al.\* \(2001\)](#), see also [Tassin \*et al.\* \(2013\)](#) and [Korobkin \*et al.\* \(2017a\)](#)).

### 5.5. Comparison with theoretical results

In this section we compare the experimental results with theoretical results obtained with different analytical models of water entry and exit. In [figure 36](#), the evolution of the wetted surface measured during the water exit experiments with the circular disc is compared with the analytical model of [Korobkin \*et al.\* \(2017a\)](#), which is an extension of the model initially proposed in [Korobkin \(2013\)](#) to an arbitrary time evolution of the acceleration of the body. In the axisymmetric version of this model, the hydrodynamic force,  $F$ , is given by the added mass and the acceleration of the body

$$F(t) = -\frac{4}{3}\rho c^3(t)\ddot{h}(t), \quad (5.1)$$

and the evolution of the radius of the contact surface,  $c(t)$ , is governed by the following differential equation

$$\frac{dc}{dt} = -\frac{2}{\pi}\gamma c(t) \int_{t_1}^t \frac{\ddot{h}(\tau) d\tau}{\sqrt{c^2(\tau) - c^2(t)}}, \quad (5.2)$$

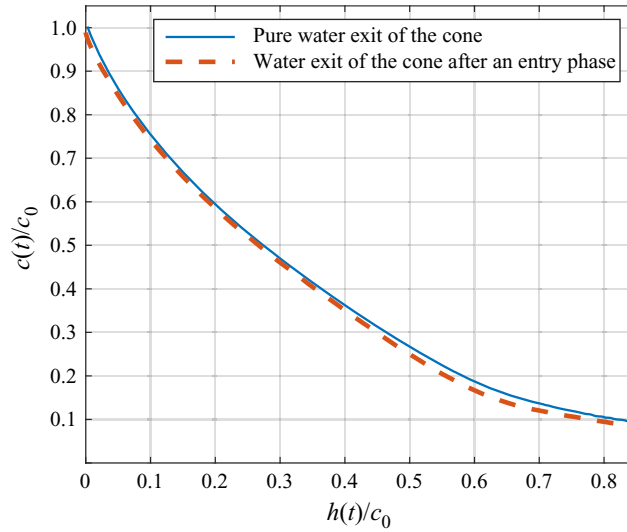


FIGURE 34. Evolution of the non-dimensional radius of the wetted surface  $c(t)/c_0$  as a function of the non-dimensional elevation  $h(t)/c_0$  with  $c_0 = 200$  mm.

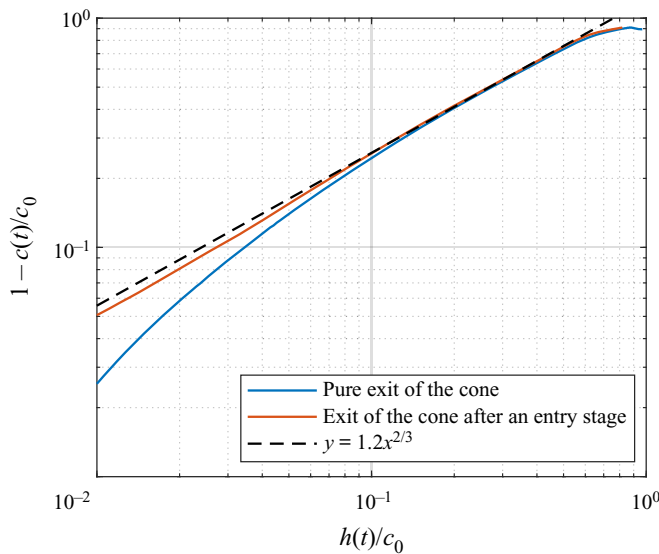


FIGURE 35. Evolution of the non-dimensional radius of the wetted surface  $c(t)/c_0$  as a function of the non-dimensional elevation  $h(t)/c_0$  with  $c_0 = 200$  mm and in log–log scale.

where  $t_1 = -\infty$  for the pure water exit experiments and  $t_1 = t_0 + T/4$  in the combined water entry and exit experiments. We follow the methodology proposed in Korobkin *et al.* (2017a) to solve (5.2), but once the solution is well initialized, we solve directly (5.2) with a standard first-order explicit Euler integration scheme because the methodology proposed in Korobkin *et al.* (2017a) is no longer valid when the body acceleration  $\dot{h}(t)$  is equal to 0. It is important to have in mind that gravity effects are neglected in this model, but quantitative comparisons with the experimental results can be made during the early stage

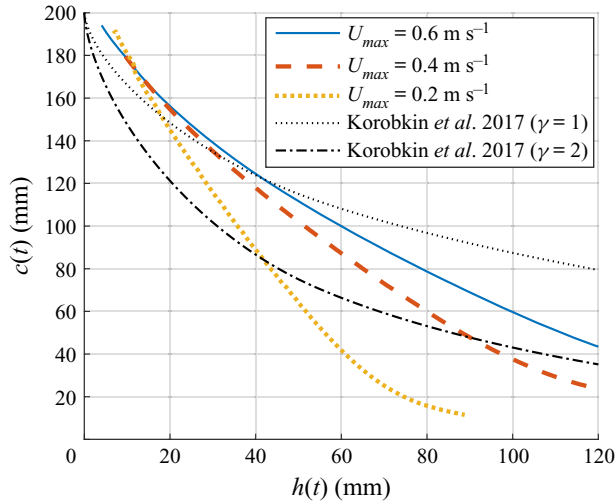


FIGURE 36. Comparison between the wetted surface radius predicted by the model of Korobkin et al. (2017a) and the one measured during the water exit of the disc.

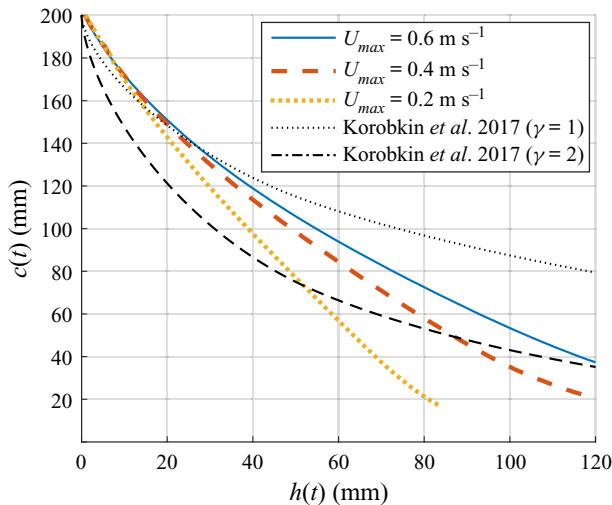


FIGURE 37. Comparison between the wetted surface radius predicted by the model of Korobkin et al. (2017a) and the one measured during the water exit of the cone.

of the exit. Indeed, the very close agreement between the experimental results obtained for  $U_{max} = 0.6 \text{ m s}^{-1}$  and  $U_{max} = 0.4 \text{ m s}^{-1}$  for  $h(t) < 30 \text{ mm}$  indicates that gravity has very little effect on the evolution of the wetted surface during this stage. The theoretical results obtained with  $\gamma = 1$  are closer to the experimental results obtained for  $U_{max} = 0.6 \text{ m s}^{-1}$  and  $U_{max} = 0.4 \text{ m s}^{-1}$  at the beginning of the exit, but the theoretical model overestimates the width of the wetted surface as the elevation increases. This divergence between the theoretical and the experimental results is due to the gravity effect which increases as  $h(t)$  increases. With  $\gamma = 2$ , the theoretical model seems to underestimate significantly the width of the wetted surface. From figure 36, it seems that there is a slight shift between the experimental and theoretical (for  $\gamma = 1$ ) wetted surface radius evolutions. The reason for

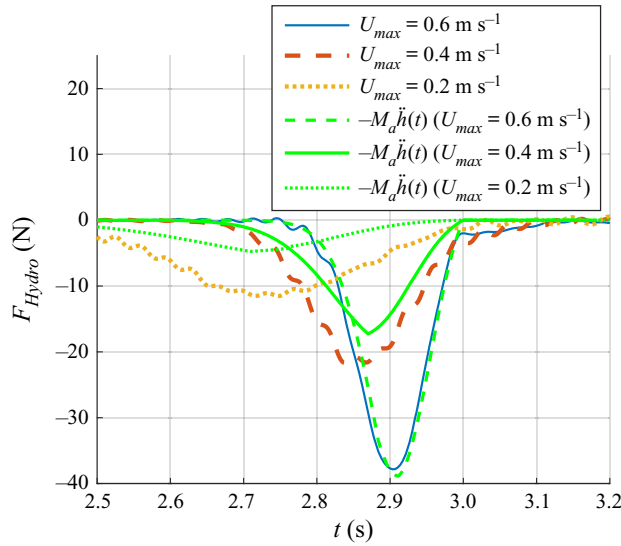


FIGURE 38. Comparison between the hydrodynamic force predicted by the linearized added mass approach and the one measured during the water exit of the disc.

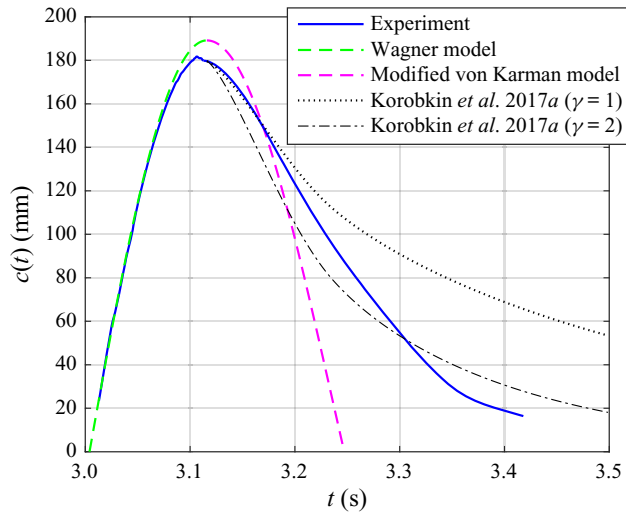


FIGURE 39. Evolution of the radius of the wetted area for the water entry and exit of a cone with  $U_{max} = 0.57 \text{ m s}^{-1}$  and  $c_{max} = 200 \text{ mm}$ .

that is probably due to the fact that the initial value of the wetted surface in the experiments is slightly larger than the disc radius, because of the presence of a meniscus (see figure 6). The same problem does not occur during the water exit of the cone because the initial altitude of the mock-up was adjusted such as to have the desired value of  $c_0$  (see § 2.3). Figure 37 presents a comparison between the predictions of the linearized water exit model of Korobkin *et al.* (2017a) and the experimental wetted surface evolutions obtained with the cone for different exit velocities. For low values of the elevation  $h(t)$ , the evolution of the wetted surface radius is independent of the exit velocity. This corresponds to the stage where gravity effects are negligible. During this stage, the results obtained from the model

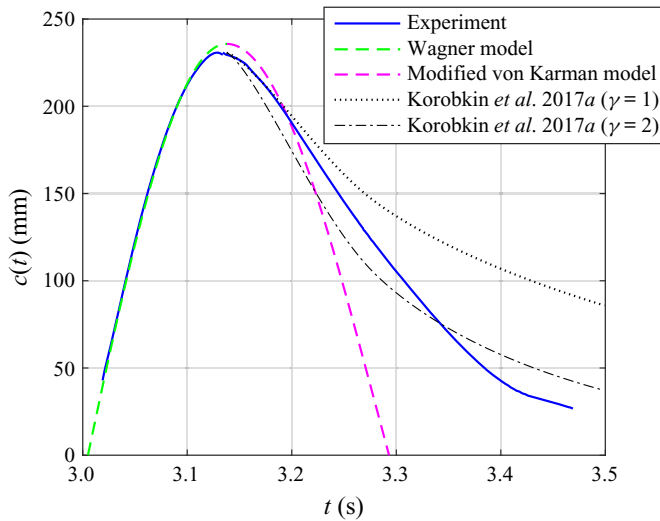


FIGURE 40. Evolution of the radius of the wetted area for the water entry and exit of a cone with  $U_{max} = 0.6 \text{ m s}^{-1}$  and  $c_{max} = 250 \text{ mm}$ .

of Korobkin *et al.* (2017a) with  $\gamma = 1$  are in excellent agreement with the experimental results. In figure 38, we compare the hydrodynamic force measured during the water exit of the circular disc with the hydrodynamic force predicted by the added mass approach (5.1) and using the value of  $c(t)$  measured during the experiments. Note that we were not able to measure the width of the wetted surface at the very beginning of the experiments, so we used the first measured value of  $c(t)$  to calculate the hydrodynamic force at the beginning of the exit. Figure 38 shows that the added mass approach seems to provide a good prediction of the hydrodynamic force for the largest values of  $U_{max}$ . For smaller exit velocities, the added mass approach largely underestimates the hydrodynamic force. The reason of these differences is very likely related to the influence of gravity, which is not included in the added mass approach. However, the measured hydrodynamic force still follows a time evolution similar to the time evolution of the acceleration, despite the fact that the magnitude of the body acceleration is much smaller than the gravity acceleration for  $U_{max} = 0.2 \text{ m s}^{-1}$  (see figure 7b).

In figures 39 and 40, the evolution of the radius of the wetted surface measured during the water entry and exit of the cone is compared with the theoretical prediction of the radius of the wetted surface obtained from the combined Wagner-modified von Karman model. This model was proposed by Tassin *et al.* (2013) for the two-dimensional case and is directly applicable to the axisymmetric case. When computing the theoretical results, we assumed that the altitude of the tip of the cone,  $z$ , was given by the equation  $z = h(t) + \delta_z$  with  $\delta_z = 3 \text{ mm}$  in order to compensate for the meniscus (see § 2.3), leading to  $c(t) = -4[\delta_z + h(t)]/[\pi \tan(15^\circ)]$ . The results obtained from the Wagner model compare remarkably well with the experimental results during the entry stage, despite the fact that the Wagner model does not take into account the gravity in the computation of the radius of the wetted surface. However, the agreement between the modified von Karman model and the experimental results is significantly less satisfactory during the exit stage. The results obtained from the model of Korobkin *et al.* (2017a) for  $\gamma = 1$  and  $\gamma = 2$  are also depicted in figures 39 and 40. For these last results, the wetted surface at the beginning of the exit stage (when  $\dot{h}(t) = 0$ ) was set to the experimental value. The wetted surface

evolutions obtained with  $\gamma = 1$  are very close to the experimental data at the beginning of the exit stage, but the theoretical model overestimates the wetted surface at the end of the exit stage because of the effect of gravity. Note, however, that Korobkin (2013) found that a value of  $\gamma = 2$  led to a better prediction of the hydrodynamic force for large values of body elevation (when compared with numerical results obtained from a CFD approach). In order to improve the linearized model so as to get a consistent prediction of the hydrodynamic force and of the wetted surface, it seems necessary to improve the hydrodynamic force/pressure formulation.

## 6. Conclusion and discussion

In this paper, we have presented an experimental study on the water exit and entry–exit of axisymmetric bodies both flat and three-dimensional. The experimental set-up makes it possible to measure simultaneously the evolution of the wetted surface and of the hydrodynamic force. The LED edge-lighting technique proposed in Tassin *et al.* (2017) was employed to track the evolution of the wetted surface. We have now demonstrated the feasibility of the LED edge-lighting technique in a medium-scale wave tank with mock-ups of sizes up to 50 cm diameter. The accuracy of the technique was validated through comparisons with experiments during which a draughtboard was placed at the bottom of the tank. The LED technique makes it possible to track the contact line during the water exit of axisymmetric bodies both flat and three-dimensional. During the water entry stage of three-dimensional bodies, it is possible to observe simultaneously the contact line and the front of the jet, which is a remarkable advantage compared with the standard approach based on the use of non-transparent mock-ups.

The obtained results provide different insights on the physics of the water entry phenomenon. The experiments conducted in Froude similarity with different values of the initial radius of the wetted surface show that the similarity is verified. This indicates that viscosity and surface tension do not have a significant influence in the present experiments (except for the presence of the meniscus). Our experiments confirm that the shape of the body does not play an important role in the evolution of the contact surface during water exit. The experimental results show that the evolution of the contact surface during an exit stage which follows an entry stage is very similar to the one observed during a pure water exit experiment. It is also interesting to notice that for the experiments with the largest velocity ( $U_{max} = 0.6 \text{ m s}^{-1}$ ), the evolution of the contact line follows a similar law as the theoretical prediction of the self-similar model of Korobkin *et al.* (2017b).

The results of the water entry experiments have been compared with the predictions of the Wagner model. It was shown that it is possible to predict very accurately the evolution of the radius of the wetted surface with the Wagner model, despite the influence of gravity in our experiments. For the exit stage, the results obtained with the modified von Karman model are much less satisfactory. An extension of the linearized water exit model of Korobkin *et al.* (2017a) has been implemented in order to model the water exit of a rigid axisymmetric body with an arbitrary exit kinematics ( $\dot{h}(t) \geq 0$ ). The theoretical results obtained from this model with  $\gamma = 1$  are in good agreement with the experimental results at the beginning of the exit stage (when the effect of gravity is negligible). However, the theoretical model overestimates the wetted surface when the elevation and the effect of gravity increase. It is interesting to note that the exit stage seems to be more affected by gravity than the entry stage.

An original aspect of the experimental set-up used in the present study is that the evolution of the surface of contact between the solid and the liquid is tracked using an optical method based on the use of a LED edge-lighting technique and



transparent mock-ups. This method offers several advantages compared with the draughtboard technique or to the use of opaque mock-ups. The LED technique can be used in large and deep basins, which is less convenient with the two other techniques. With the LED edge-lighting technique, the video camera is in air whereas with opaque mock-ups it is necessary to use an underwater camera or mirrors when possible. The edge-lighting technique makes it possible to track simultaneously the contact line and the jet front during the entry stage, which is not possible with opaque mock-ups. It is most likely possible to apply the LED edge-lighting technique to mock-ups subject to a rotation (e.g. pitch motion), which would be nearly impossible with the draughtboard technique.

The LED edge-lighting technique has nevertheless a few disadvantages. In particular, the mock-up and the water have to be clean. The intensity of the light is rather low which necessitates the high-speed video camera to have a good light sensitivity. The surface of the mock-ups has to be very finely polished.

In future, we are planning to apply this technique to more complex motions including rotations and to freely moving mock-ups (e.g. sea-keeping experiments). Eventually, we would like to study wave impacts on three-dimensional shapes (promising preliminary results have been obtained with the sphere). The edge-lighting technique may be used for other applications where the tracking of the contact line and of the jet front are important (e.g. droplet impacts on solid substrates, sloshing in tanks). Additional results on the water exit of an elliptical disc and of a square plate should be published soon.

### Acknowledgements

T.B. and A.T. acknowledge the technical assistance of S. Chalony from Ifremer for his help in designing, preparing and conducting the experiments. T.B. and A.T. acknowledge the team members of Ifremer's wave and current flume in Boulogne-sur-Mer for their assistance during the two experimental campaigns. The authors would like thank Dr R. Hascoët from ENSTA Bretagne for his careful reading of the manuscript before submission. D. Le Roux from Ifremer contributed to the initial design of the experimental set-up. The experimental set-up was funded by Institut Carnot Ifremer-EDROME. This work was also supported by Région Bretagne (ARED funding) through the PhD grant of T.B.

### Declaration of interests

The authors report no conflict of interest.

### Appendix A. Validation of the LED edge-lighting technique for the different mock-ups

In this appendix, we compare the results obtained with the LED edge-lighting technique and the results obtained with the draughtboard technique in order to assess the accuracy of the edge-lighting technique for the tracking of the contact line during the water exit experiments with the different shapes. All the images depicted in this section were captured at a frame rate of 1000 f.p.s.. The online version of the article can be used to zoom in on small details of the images.

#### A.1. Water exit of the circular disc

A sequence of four images recorded during the water exit of the circular disc for different values of the elevation,  $h(t)$ , is plotted in [figure 41](#). In these images, the inner illuminated

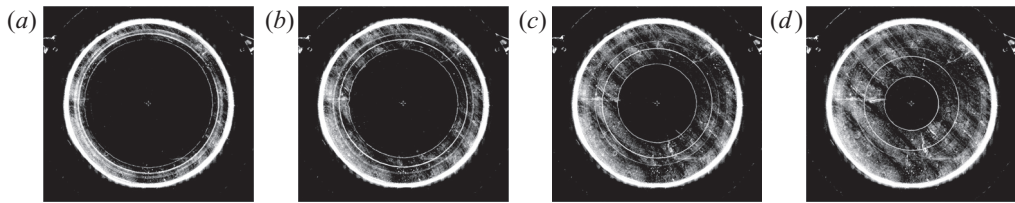


FIGURE 41. Sequence of images recorded during the water exit of the 200 mm radius circular disc with the LED edge-lighting technique for  $U_{max} = 0.6 \text{ m s}^{-1}$ : (a)  $h = 18.0 \text{ mm}$ ,  $h = 33.0 \text{ mm}$ ,  $h = 61.4 \text{ mm}$  and (d)  $h = 91.4 \text{ mm}$ .

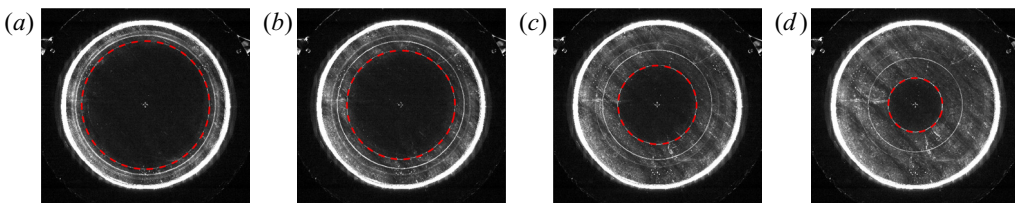


FIGURE 42. Detection of the contact line (red dashed line) from the images obtained with the LED edge-lighting technique during the water exit of the 200 mm radius circular disc with the LED edge-lighting technique for  $U_{max} = 0.6 \text{ m s}^{-1}$ : (a)  $h = 18.0 \text{ mm}$ , (b)  $h = 33.0 \text{ mm}$ , (c)  $h = 61.4 \text{ mm}$  and (d)  $h = 91.4 \text{ mm}$ .

ring which contracts towards the centre of the image as the elevation increases corresponds to the contact line. The outer concentric rings are attributed to the direct diffusion of light due to the imperfect polishing of the sides of the mock-up and to undesired specular reflections of the light source on the deformed free surface. Similarly to the results presented in § 3.2 for the water entry and exit of the cone, the contact line geometry is extracted using a contour detection algorithm based on the method of Taubin (1991) and assuming that the shape of the contact line is elliptic. The performance of the contour tracking algorithm is illustrated in figure 42 where the detected contours and the original images (from figure 41) are superimposed.

In order to verify that the inner ring corresponds to the contour of the wetted surface (the contact line), the same experiments were conducted with a draughtboard laying at the bottom of the tank (approximately 2 m below the free surface). With this technique, the region over which the water is in contact with the mock-up corresponds to the region over which the draughtboard appears undistorted (see figure 43). The red dashed line which is superimposed to the images obtained with the draughtboard technique in figure 43 corresponds to the contour extracted from figure 42. One can observe that the region over which the draughtboard remains undistorted is perfectly circumscribed by the contour extracted from figure 42. This comparison demonstrates the accuracy of the LED edge-lighting technique in the case of the circular disc.

#### A.2. Water exit of the cone

The same verification was performed for the cone. A sequence of images obtained during the water exit of the cone with an initial radius of the wetted surface  $c_0 = 200 \text{ mm}$  is depicted in figure 44. Similarly to the images obtained during the water exit of the circular disc, one can observe an inner illuminated ring which contracts towards the centre of

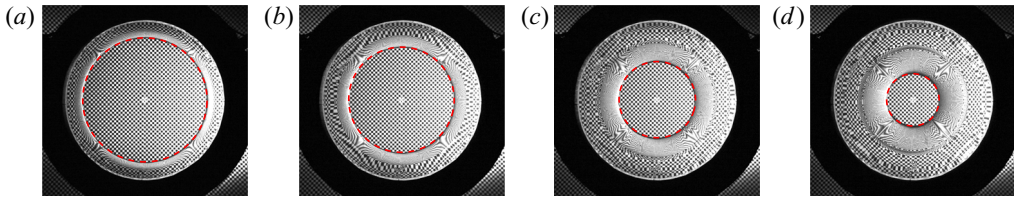


FIGURE 43. Comparison between the contact line obtained with the LED edge-lighting technique (red dashed line) and the images obtained with the draughtboard during the water exit of the 200 mm radius circular disc for  $U_{max} = 0.6 \text{ m s}^{-1}$ : (a)  $h = 18.0 \text{ mm}$ , (b)  $h = 33.0 \text{ mm}$ , (c)  $h = 61.4 \text{ mm}$  and (d)  $h = 91.4 \text{ mm}$ .

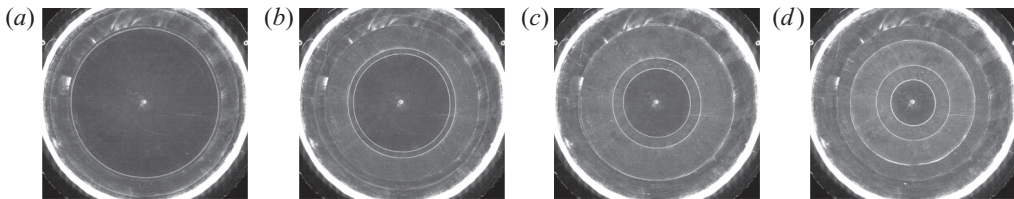


FIGURE 44. Sequence of images recorded during the water exit of the cone with an initial value of the radius of the wetted surface  $c_0 = 200 \text{ mm}$  for  $U_{max} = 0.6 \text{ m s}^{-1}$ : (a)  $h = 2.4 \text{ mm}$ , (b)  $h = 31.5 \text{ mm}$ , (c)  $h = 60.8 \text{ mm}$  and (d)  $h = 90.8 \text{ mm}$ .

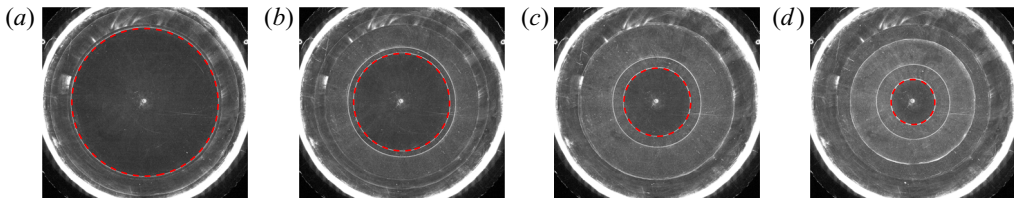


FIGURE 45. Detection of the contact line (red dashed line) from the images obtained with the LED edge-lighting technique during the water exit of the cone initially in contact with the water on a surface of radius  $c_0 = 200 \text{ mm}$  for  $U_{max} = 0.6 \text{ m s}^{-1}$ : (a)  $h = 2.4 \text{ mm}$ , (b)  $h = 31.5 \text{ mm}$ , (c)  $h = 60.8 \text{ mm}$  and (d)  $h = 90.8 \text{ mm}$ .

the image. Note that the tip of the cone coincides with the bright dot which is visible at the centre of the images. The contours extracted from these images are plotted in [figure 45](#) and superimposed to the images obtained with the draughtboard technique during the water exit of the cone in [figure 46](#). One observes that the contour illuminated with the LED edge-lighting technique closely corresponds to the contour of the region over which the draughtboard is distorted only by the conical shape of the mock-up.

### A.3. Water exit of the sphere

A sequence of four images obtained during the water exit of the sphere with the LED edge-lighting technique is plotted in [figure 47](#). Note that the position of the axis of symmetry is marked by a bright dot at the centre of the mock-up. The contours extracted from these images are superimposed to the original images in [figure 48](#) and to the images obtained with the draughtboard technique in [figure 49](#). One can appreciate the close correlation between the contact line illuminated with the LED edge-lighting technique

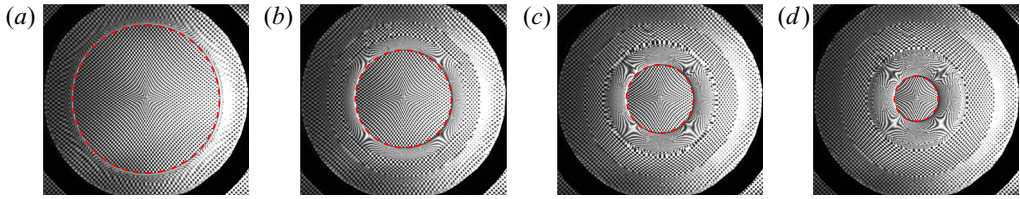


FIGURE 46. Comparison between the contact line obtained with the LED edge-lighting technique (red dashed line) and the images obtained with the draughtboard technique during the water exit of the cone initially in contact with the water on a surface of radius  $c_0 = 200$  mm for  $U_{max} = 0.6$  m s $^{-1}$ : (a)  $h = 2.4$  mm, (b)  $h = 31.5$  mm, (c)  $h = 60.8$  mm and (d)  $h = 90.8$  mm.

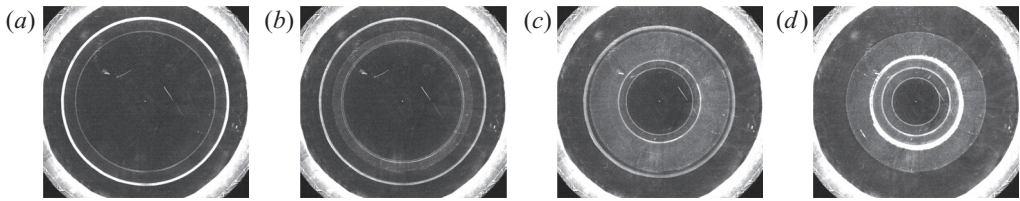


FIGURE 47. Sequence of images recorded during the water exit of the sphere with an initial value of the radius of the wetted surface  $c_0 = 200$  mm for  $U_{max} = 0.6$  m s $^{-1}$ : (a)  $h = 0.3$  mm, (b)  $h = 10.9$  mm, (c)  $h = 60.8$  mm and (d)  $h = 90.8$  mm.

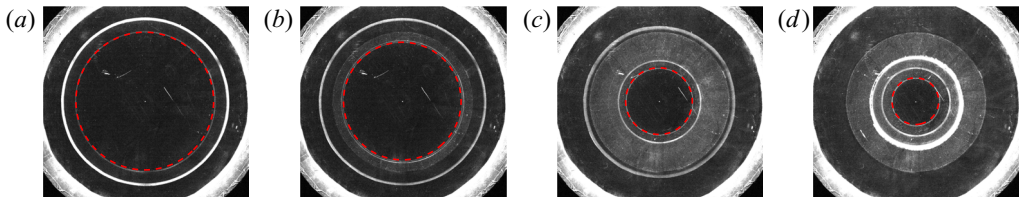


FIGURE 48. Detection of the contact line (red dashed line) from the images obtained with the LED edge-lighting technique during the water exit of a sphere initially in contact with the water on a surface of radius  $c_0 = 200$  mm for  $U_{max} = 0.6$  m s $^{-1}$ : (a)  $h = 0.3$  mm, (b)  $h = 10.9$  mm, (c)  $h = 60.8$  mm and (d)  $h = 90.8$  mm.

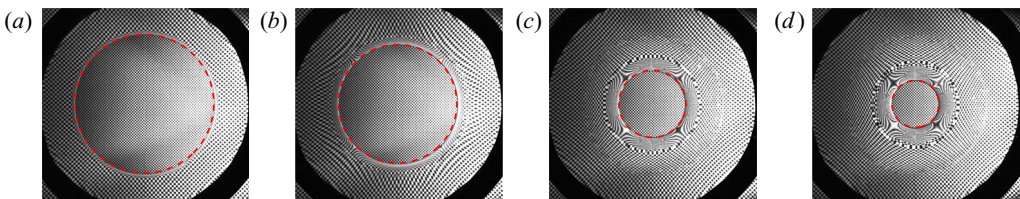


FIGURE 49. Comparison between the contact line obtained with the LED edge-lighting technique (red dashed line) and the images obtained with the draughtboard during the water exit of a sphere initially in contact with the water on a surface of radius  $c_0 = 200$  mm for  $U_{max} = 0.6$  m s $^{-1}$ : (a)  $h = 0.3$  mm, (b)  $h = 10.9$  mm, (c)  $h = 60.8$  mm and (d)  $h = 90.8$  mm.

and the contour of the wetted surface obtained with the draughtboard technique. It should be noted that in the case of the sphere, the tracking of the luminous contour is made a bit more difficult at the beginning of the exit because of the presence of a secondary luminous

ring very close to the contour of interest and which may be mistaken for the contact line by the tracking algorithm. The results obtained with the LED edge-lighting technique remain nevertheless very accurate in the case of the sphere.

## REFERENCES

- BAARHOLM, R. & FALTINSEN, O. M. 2004 Wave impact underneath horizontal decks. *J. Mar. Sci. Technol.* **9**, 1–13.
- BENSCH, L., SHIGUNOV, V., BEUCK, G. & SÖDING, H. 2001 Planned ditching simulation of a transport airplane. In *KRASH USERS SEMINAR, 7–10 January 2001, Phoenix, Arizona*.
- DUEZ, C., YBERT, C., BARENTIN, C., COTTIN-BIZONNE, C. & BOCQUET, L. 2008 Dynamics of Fakir liquids: from slip to splash. *J. Adhes. Sci. Technol.* **22**, 335–351.
- EL MALKI ALAOU, A., NÈME, A., TASSIN, A. & JACQUES, N. 2012 Experimental study of slamming coefficients during vertical water entry of axisymmetric rigid shapes at constant speeds. *Appl. Ocean Res.* **37**, 183–197.
- HALBOUT, S. 2011 Contribution à l'étude des interactions fluide-structure lors de l'impact hydrodynamique avec vitesse d'avance d'un système de flottabilité d'hélicoptère (in french). PhD thesis, Université d'Aix-Marseille, France.
- IAFRATI, A. & GRIZZI, S. 2019 Cavitation and ventilation modalities during ditching. *Phys. Fluids* **31** (5), 052101.
- KAPLAN, P. 1987 Analysis and prediction of flat bottom slamming impact of advanced marine vehicles in waves. *Intl Shipbuilding Prog.* **34** (391), 44–53.
- KOROBKIN, A. A. 2007 Second-order Wagner theory of wave impact. *J. Engng Maths* **58** (1–4), 121–139.
- KOROBKIN, A. A. 2013 A linearized model of water exit. *J. Fluid Mech.* **737**, 368–386.
- KOROBKIN, A. A. & SCOLAN, Y.-M. 2006 Three-dimensional theory of water impact. Part 2. Linearized Wagner problem. *J. Fluid Mech.* **549**, 343–373.
- KOROBKIN, A., KHABAKHPASHEVA, T. & MAKI, K. 2017a Hydrodynamic forces in water exit problems. *J. Fluids Struct.* **69**, 16–33.
- KOROBKIN, A., KHABAKHPASHEVA, T. & RODRÍGUEZ-RODRÍGUEZ, J. 2017b Initial stage of plate lifting from a water surface. *J. Engng Maths* **102**, 117–130.
- PANCIROLI, R., ABRATE, S., MINAK, G. & ZUCHELLI, A. 2012 Hydroelasticity in water-entry problems: comparison between experimental and SPH results. *Compos. Struct.* **94** (2), 532–539.
- PIRO, D. J. & MAKI, K. J. 2013a An adaptive interface compression method for water entry and exit. *Tech. Rep.* 2013-350. University of Michigan Department of Naval Architecture and Marine Engineering.
- PIRO, D. J. & MAKI, K. J. 2013b Hydroelastic analysis of bodies that enter and exit water. *J. Fluids Struct.* **37**, 134–150.
- REINHARD, M. 2013 Free elastic plate impact into water. PhD thesis, University of East Anglia, UK.
- REINHARD, M., KOROBKIN, A. A. & COOKER, M. J. 2012 The bounce of a blunt body from a water surface at high horizontal speed. In *27th International Workshop on Water Waves and Floating Bodies. 22–25 April 2012, Copenhagen, Denmark*.
- REIS, P. M., JUNG, S., ARISTOFF, J. M. & STOCKER, R. 2010 How cats lap: water uptake by felis catus. *Science* **330**, 1231–1234.
- SCOLAN, Y.-M., REMY, F. & THIBAUT, B. 2006 Impact of three-dimensional standing waves on a flat horizontal plate. In *21st International Workshop on Water Waves and Floating Bodies. 2–5 April 2006, Loughborough, U.K.*
- SEMOV, Y. A. & YOON, B.-S. 2009 Onset of flow separation for the oblique water impact of a wedge. *Phys. Fluids* **21**, 112103.
- SHAMS, A., ZHAO, S. & PORFIRI, M. 2017 Hydroelastic slamming of flexible wedges: modeling and experiments from water entry to exit. *Phys. Fluids* **29** (3), 037107.
- SUN, H. & HELMERS, J. B. 2015 Slamming loads on a wedge elastically suspended on a marine structure. In *ASME 2015 34th International Conference on Ocean, Offshore and Arctic Engineering*. American Society of Mechanical Engineers.
- TANG, Z., VON GIOI, R. G., MONASSE, P. & MOREL, J.-M. 2017 A precision analysis of camera distortion models. *IEEE Trans. Image Process.* **26**, 2694–2704.

- TASSIN, A., BRETON, T., FOREST, B., OHANA, J., CHALONY, S., LE ROUX, D. & TANCRAZ, A. 2017 Visualization of the contact line during the water exit of flat plates. *Exp. Fluids* **58** (8), 104.
- TASSIN, A., JACQUES, N., EL MALKI ALAOU, A., A. NÈME & B. LEBLÉ 2012 Hydrodynamic loads during water impact of three-dimensional solids: modelling and experiments. *J. Fluids Struct.* **28**, 211–231.
- TASSIN, A., PIRO, D. J., KOROBKIN, A. A., MAKI, K. J. & COOKER, M. J. 2013 Two-dimensional water entry and exit of a body whose shape varies in time. *J. Fluids Struct.* **40**, 317–336.
- TAUBIN, G. 1991 Estimation of planar curves, surfaces, and nonplanar space curves defined by implicit equations with applications to edge and range image segmentation. *IEEE Trans. Pattern Anal. Mach. Intell.* **13** (11), 1115–1138.
- VEGA-MARTÍNEZ, P., RODRÍGUEZ-RODRÍGUEZ, J., KHABAKHPASHEVA, T. & KOROBKIN, A. 2019 Hydro-elastic effects during the fast lifting of a disc from a water surface. *J. Fluid Mech.* **869**, 726–751.
- WAGNER, H. 1931 Landing of seaplanes. *NACA Technical Memorandum 622*, pp. 1–23.
- WAGNER, H. 1932 Über Stoß- und Gleitvorgänge an der Oberfläche von Flüssigkeiten. *Z. Angew. Math. Mech.* **12**, 193–215 (in German).